Joint Seminar Series Summaries

NOAA Climate Test Bed
Center for Ocean-Land-Atmosphere Studies
UMCP Earth System Science Interdisciplinary Center
UMCP Department of Atmospheric and Oceanic Science
NASA/GSFC Global Modeling and Assimilation Office

Assessment of Improvement in Climate Prediction with Outstanding R&D Needs

Office of Science and Technology

NOAA's National Weather Service

2010

Office of Science and Technology
National Weather Service
National Oceanic and Atmospheric Administration
U.S. Department of Commerce

http://www.nws.noaa.gov/ost/climate/STIP/fy10jsctb.htm

TABLE OF CONTENT

SYNTHESIS

The 2009-2010 NOAA Climate Test Bed Joint Seminar Series co-hosted by NOAA Climate Test Bed, COLA/GMU, ESSIC/UMCP and GSFC/NASA, spanned the period 19 October 2009 to 1 June 2010. Thirteen speakers, eleven from host institutions and two invitees from Princeton University and Georgia Institute of Technology (GIT), presented talks during the series.

I. Ocean model and data assimilation

The NCEP Global Ocean Data Assimilation System (GODAS) pentad products have been used for monitoring ENSO at CPC in near real-time. According to an assessment by the CPC ocean monitoring group, the GODAS heat budget closure is good for weak-to-moderate El Niño but poor for strong La Niña. Additional research support is needed especially in the areas of (1) assimilation of observed salinity to reduce large biases in zonal and meridional currents, thus improving the annual cycle of advective heat fluxes; (2) multi-model analysis, which will not only reduce uncertainty in the analysis but also focus requirements for the ocean observing system for the operational data streams.

ENSO is one of the important predictors used by NWS forecasters to make ISI climate prediction. Studies show bio-climate interaction in the tropical Pacific has significant effects on ENSO variability, which hasn't been included in CFS so far. ESSIC research experiments demonstrate a way of parameterizing the mechanism to be applied for CFS. It is anticipated that ocean biology in the tropical Pacific would contribute to the modulation of the mean climate and ENSO development through the penetrative effect on solar radiation, leading to an improved climate forecast.

II. Land model and data assimilation

The impacts of the NCEP land model (Noah/GLDAS) on CFS forecasts of US summer season precipitation are considerable in preferred regions. The ocean coupling plays an important role in amplifying the positive impact over land via the atmospheric bridge. An assessment by the EMC land modeling group showed that the low quality of wintertime soil moisture assimilation data was due to the inability of the model to simulate frozen soil and snowmelt processes. The current system needs to be extended to multiple land models and use multiple coupled GCM forecast products to improve forcing reliability. The current land data assimilation system is a pseudo assimilation system, meaning it does not really assimilate observed land data. Additional research to assimilate observed land states (*e.g.* soil moisture, surface temperature, streamflow *etc.*) using available satellite and in-situ data with modern data assimilation techniques is required.

III. Predictability and prediction

Is the spring predictability barrier intrinsic to the climate system or a model problem? COLA research demonstrates that excessive persistence or delayed phase transition associated with wind stress structural errors is a likely cause of the spring prediction barrier in CFS, suggesting that the barrier is largely due to model deficiencies. By improving the atmospheric model wind stress response to SST anomalies, an improvement in ENSO forecast skill is expected.

The predictability of tropical cyclones (TC) is linked to deep-layer wind shear and to the frequency of easterly waves. ECMWF monthly forecasts have the ability to isolate active/break periods for TC activity on intraseasonal time scales as well as TC genesis from easterly waves in the Atlantic hurricane main development region (MDR) through three weeks. The TC forecast on intraseasonal time scales will improve further with better simulations of the MJO phase and amplitude.

For predicting meteorological drought, the CPC drought monitoring group uses the Standardized Precipitation Index (SPI) to avoid land model errors. By comparing four different statistical downscaling methods (including two developed by major research partners in Princeton University and University of Washington) and a dynamical downscaling approach, it is

concluded that significant gain of precipitation forecast skill cannot be expected by increasing the model resolution alone, which emphasizes the need to focus on model physics to address model bias.

Drought research at GSFC indicates that for hydrological drought, the soil moisture information contributes to skillful seasonal forecast of the snowmelt-season streamflow. Improving soil moisture initialization is as important as improving snow initialization. For agriculture drought, model dependent soil moisture memory and forecast methodology are two key aspects to improve soil moisture forecasts. Precipitation is the most important forcing among meteorological forcing fields. For meteorological drought, climate dynamics plays a significant role in multi-year drought prediction.

The NCEP CFS monsoon simulations analyzed by the CPC monsoon group demonstrate that high resolution and coupling with oceans significantly improves CFS simulations of the Asian monsoon characteristics, indicating the importance of small scale feedbacks and ocean-atmosphere interactions. The distinct improvement of predicting East Asian winter monsoon and East Asian Mei-yu would benefit predictions of system development downstream, which needs to be explored. Outstanding R&D needs include: (1) understanding the impact of complex regional topography on precipitation and circulation simulations, (2) role of land physics in determining the sea-land contrast that influences the monsoon strength, and (3) improving ENSO-monsoon relationship, which is working in the model but is too strong.

The CFS forecast skill and predictability of the South Asian monsoon and South American monsoon have been assessed by COLA on daily and intraseasonal time scales and for forecasts initiated in different months of the monsoon seasons. The doubling time of small predictability errors for the South Asian monsoon is found to be in the range of 4-7 days for forecasts initiated in July whereas it is in the range of 5-14 days for forecasts starting in May. Examination of the growth of forecast errors, which start from different phases of the monsoon intraseasonal variability, shows that for the rainfall averaged over the land points of India, the forecast errors grow faster in the case of forecasts being initiated during active or break phases, while they grow slower with forecasts starting from normal phase. The South American monsoon predictability has been assessed by examining the error growth of the dominant modes of the rainfall variability. It is found that the ENSO rainfall mode has very slow growth rate, providing a basis for better predictability of certain features of the rainfall over South America. In the case of the intraseasonal mode, which propagates northeastward, the error growth is slow but with oscillatory behavior, reflecting the fact that the phases of the propagation are not properly simulated.

IV. Advisory

The societal needs for the earth system prediction are at two distinct time and spatial scales (days to seasons at resolutions of order meters versus years to decades at macroscopic spatial scale). To support sustainable resource management on a day-to-day basis, ESSIC research emphasizes improving regional earth prediction systems and the observation network and advises CTB to make multidisciplinary connections, paying more attention to important feedback processes between the physical climate system and the terrestrial and marine biogeo-chemistry and ecosystems.

(By Jiayu Zhou, E-mail: Jiayu.Zhou@noaa.gov; Wayne Higgins and Fiona Horsfall)

---

* Interested readers are encouraged to visit the seminar series web page located at http://www.weather.gov/ost/climate/STIP/fy10jsctb.htm. The web page provides links to presentation files and contributed extended summaries.

US National Oceanic and Atmospheric Administration
Climate Test Bed Joint Seminar Series
NCEP, Camp Springs, Maryland, 3 November 2009

Ocean Biology-Induced Climate Feedback Effects on Interannual Variability in the Tropical Pacific: A Missing Process in the NCEP CFS

Rong-Hua Zhang and Antonio J. Busalacchi
Earth System Science Interdisciplinary Center (ESSIC)
University of Maryland, College Park, MD

ABSTRACT

Satellite-based ocean color measurements indicate clear evidence for bio-climate interactions in the tropical Pacific associated with El Niño-Southern Oscillation (ENSO). Recent data analyses and modeling studies have demonstrated that ocean biology can potentially affect the climate in the tropical Pacific through the penetration depth of solar radiation in the upper ocean (H_p), a field serving as a link between the climate system and the marine ecosystem. However, most global climate models, including the NCEP CFS, have not adequately taken into account ocean biology-induced heating effects. In particular, interannually varying effect of H_p on the heat budget has not been included. Therefore, the ocean biology-induced feedback (OBF) to the physics and the corresponding coupled bio-climate interactions are still missing in the NCEP CFS. It is very unlikely that in the near-term the CFS will include a comprehensive ocean biogeochemical model to resolve interannual H_p variability. Furthermore, great difficulties still exist in capturing interannual H_p variability using physical and biological ocean models. For example, current comprehensive and time-consuming ocean biogeochemistry models still can not realistically depict interannual H_p anomalies during ENSO cycles. A cost-effective parameterization is clearly needed to take into account the ocean biology-induced heating effect on the upper ocean; a key is to explicitly capture interannual H_p variability which is dominantly forced by ENSO in the tropical Pacific.

Over the past decade, remote sensing has led to significant advances in physical understanding, interpretation and modeling efforts of ocean biology-related effects on the climate. In particular, the time series of remotely sensed ocean color data and associated products have revolutionized how the impacts of climate variability and change on ocean biology can be understood and quantified both globally and regionally. H_p can be now accurately derived using chlorophyll content data that are available from ocean color imagery since Sep. 1997, providing an opportunity for characterizing its variability and quantifying its coherent relationships with physical fields (SST and sea level). Previously, an empirical model for interannual H_p variability has been derived using a singular value decomposition (SVD) analysis from historical satellite observations, which allows for a non-local, SST-dependent, and spatially-temporarily varying representation of H_p variability and heating effects. As a test bed, the effects of ocean biology-induced climate feedback on interannual variability in the tropical Pacific are examined by incorporating the derived empirical H_p model into a hybrid coupled ocean-atmosphere model. It is shown that the OBF has significant effects on ENSO amplitude and oscillation periods. Applications of the empirical H_p model to the NCEP CFS to represent OBF are discussed.

1. Introduction

Sunlight is the original energy source for the Earth's ocean, atmosphere, land and biosphere. Its shortwave radiation part can pass through the atmosphere relatively unimpeded and reach the Earth's surface, about 70% of which is covered by the ocean. The incoming irradiance is attenuated in the upper ocean due to pure water and due to biogenic components. Mathematically, the attenuation of incoming solar radiation follows an exponential decline with depth in the upper ocean (*e.g.*, Paulson and Simpson 1977).

Correspondence to: Rong-Hua Zhang, Earth System Science Interdisciplinary Center (ESSIC), University of Maryland, College Park, MD; E-mail: rzhang@essic.umd.edu

The penetrative solar radiation and induced heating effects on the upper layers of the ocean are controlled by different processes in the climate system and the marine ecosystem. One factor is associated with ocean biology. For example, the way in which incident solar radiation is absorbed in the mixed layer can be significantly impacted by total phytoplankton biomass and its vertical distribution. When biological activities are strong, the incoming solar irradiance attenuates strongly in the vertical with more heating being trapped in the mixed layer. When biological activities are weak, the incoming solar irradiance penetrates deeper and can directly heat subsurface layers, at the expense of the reduction of the heating in the mixed layer. Thus, the existence and variation of phytoplankton biomass can modulate the vertical penetration of solar radiation in the upper ocean (Chavez *et al.* 1998, 1999; Strutton and Chavez 2004). It has been demonstrated that ocean biology-induced heating can be an important contributor to the heat budget near the equator in the tropical Pacific (*e.g.*, Lewis *et al.* 1990; Strutton and Chavez 2004).

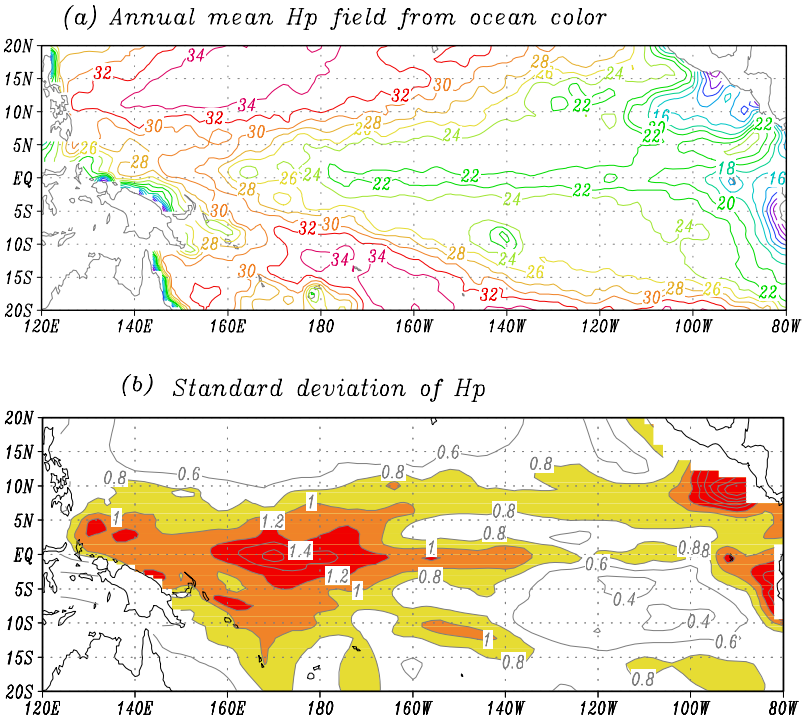

Fig. 1 The horizontal distributions of annual mean Hp field (a) and its standard deviation for interannual variability (b), estimated from the satellite ocean color data during the period Sep. 1997-Apr. 2007. The contour interval is 2 m in (a) and 0.2 m in (b).

Ocean biology-induced heating effects can be quantitatively represented by the penetration depth of solar radiation in the upper ocean (H_p), a field linking the climate system to the marine ecosystem (e.g., Murtugudde et al. 2002; Ballabrera-Poy *et al.* 2007). This field, indicating perturbations in ocean biology, exerts a direct influence on the penetrative solar radiation in the upper ocean, resulting in a differential heating in the vertical between the mixed layer and subsurface layers below, which can further lead to changes in the oceanic density field, the stability, the mixed layer depth (MLD), and vertical mixing and entrainment of subsurface cold water into the mixed layer. These oceanic processes, directly or indirectly modulated by biological conditions, can affect SST which in turn potentially feeds back to the atmosphere in the tropical Pacific where mixing and entrainment are major contributors to changes in SST. This ocean biology-induced feedback (OBF) presents additional effects on the physical system in the tropical Pacific, leading to coupled bio-physical interactions (Zhang *et al.* 2009).

Over the past decades, remote sensing has led to significant advances in physical understanding, interpretation and modeling efforts of ocean biology-induced effects on the climate. In particular, the time series of remotely sensed ocean color data and associated products have revolutionized how the impacts of ocean biology on climate variability and change can be understood and quantified both globally and regionally (*e.g.*, McCain *et al.* 1998). Satellite ocean color data are now available since 1997, which can be used to characterize basin-scale variability pattern of ocean biology and quantify its relationship with physical parameters. However, previous studies have demonstrated great sensitivities of ocean and coupled simulations to H_p specifications (*e.g.*, Nakamoto *et al.* 2001; Murtugudde *et al.* 2002; Marzeion *et al.* 2005; Manizza *et al.* 2005; Wetzel *et al.* 2006; Lengaigne *et al.* 2007; Anderson *et al.* 2007; Ballabrera-Poy *et al.* 2007; Zhang *et al.* 2009). In particular, the effects of interannual H_p variability on simulations of the mean climate and its variability in the tropical Pacific are strikingly model dependent and even conflicting.

H_p can be now derived using chlorophyll content data that are available from ocean color imagery (*e.g.*, McCain *et al.* 1998; Nakamoto *et al.* 2001; Murtugudde *et al.* 2002 and Ballabrera-Poy *et al.* 2003). Thus, satellite ocean color data-derived H_p fields can be used for ocean and coupled ocean-atmosphere modeling studies. To account for the effects of interannual H_p variability, an empirical parameterization for interannual H_p response to physical changes induced by ENSO has been developed (Zhang *et al.* 2010). The developed H_p model has been implemented into a hybrid coupled model (HCM) of the tropical Pacific and the effect on interannual variability has been examined (Zhang *et al.* 2009). These results are presented below.

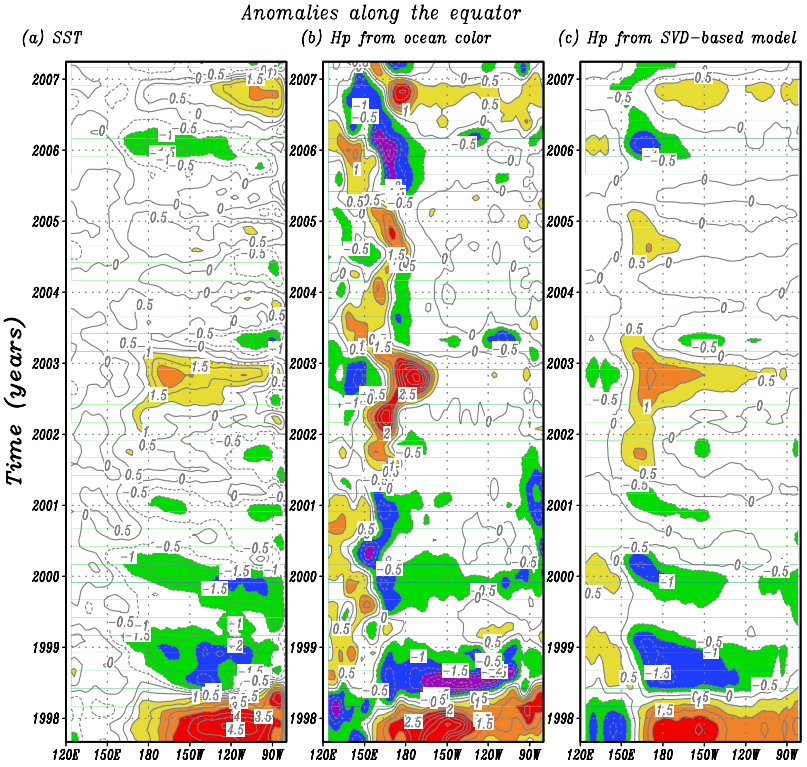

Fig. 2 Interannual anomalies along the equator during the period Sep.1997-Apr. 2007: (a) observed SST, (b) H_p derived from the ocean color data, and (c) H_p simulated from SST anomalies using the SVD-based empirical model with the first two modes retained. The contour interval is 0.5ºC in (a), and 0.5 m in (b) and (c).

2. Data and models

(1) The H_p fields derived from satellite ocean color data

Current high quality ocean color data can resolve biology-related signals in the ocean (*e.g.*, McClain *et al.* 1998), providing an opportunity for describing interannual variability in ocean biology and its coupling with physics. Following Murtugudde *et al.* (2002) and Ballabrera-Poy *et al.* (2007), the monthly H_p fields are derived from remotely sensed chlorophyll from September 1997 to April 2007.

Figure 1a illustrates the annual mean structure of the derived H_p field in the tropical Pacific (also see Murtugudde *et al.* 2002 and Ballabrera-Poy *et al.* 2003, 2007). Seasonal variations are shown in Ballabrera-Poy *et al.* (2007). The areas of small attenuation depth (<19 m) correspond to those of elevated biological activity in the coastal and equatorial upwelling regions. The Beer-Lambert law implies that regions with the smallest attenuation depth correspond to those where downwelling solar irradiance is absorbed the fastest. On interannual time scales, H_p also exhibits a basinwide signal across the tropical Pacific, which is clearly dominated by El Niño and La Niña events. A map of the standard deviation of interannual H_p variability is shown in Fig. 1b. The biology-related interannaul H_p variability is most pronounced over the central region. The standard deviation of H_p in the Niño 4 and Niño3 regions estimated from the ocean color data (Fig. 1b) is 1.14 m and 0.76 m. As H_p exhibits a clear spatial and temporal structure across the tropical Pacific basin, it exerts an influence on the penetrative solar radiation and heat balance of the mixed layer in the equatorial Pacific (*e.g.*, Lewis *et al.* 1990).

In the tropical Pacific, large interannual anomalies are evident in the SST and H_p fields (Figs. 2a-b), with their coherent co-variability pattern during ENSO cycles. For example, large-scale SST anomalies are generated by ENSO. The response in ocean biology is quick and almost simultaneous, as represented in the H_p fields whose interannual variations follow SSTs closely in the tropics (Figs. 2a-b). Clearly, both SST and H_p fields are simultaneously responding to the dynamical changes associated with ENSO; the ocean biology induced feedback impacts on SST can provide additional coupled bio-physical interactions which need to be

adequately taken into account in modeling. Since SSTs represent the forcing in terms of coupling to the atmosphere, we use SST fields to derive a feedback model relating interannual H_p variability to SST forcing.

(2) An empirical model for the attenuation depth of solar radiation (H_p)

We analyze the SST-H_p relationship on interannual time scales using SVD methods which allow to determine their statistically optimized empirical modes from their historical data (*e.g.*, Zhang *et al.* 2006). The analysis period is from September 1997 to April 2007 and the analysis domain is confined to the tropical Pacific from 25°S to 25°N and from 124°E to 76°W. The first five SVD modes explain about 54.7%, 10.2%, 7.0%, 3.7%, and 3.3% of the covariance. The spatial structure of the first derived SVD mode illustrates coherent patterns of interannual SST and H_p anomaly fields in the tropical Pacific (figures not shown).

Then, an empirical H_p model can be constructed using the derived spatial patterns of the SVD modes (see Zhang and Busalacchi (2009a) for a detailed example). Considering the sequence of the singular values and the reconstructions of interannual H_p variability from SST anomalies, only the first two SVD modes are retained (the inclusion of higher modes does not change the results significantly).

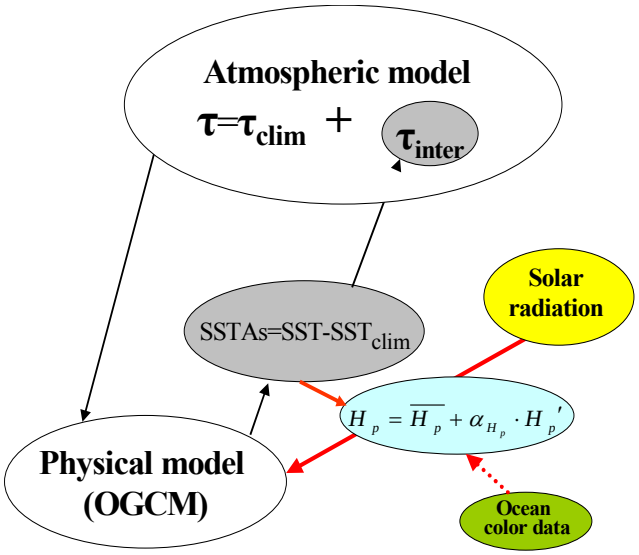

Fig. 3 A schematic illustrating a hybrid coupled model (HCM) for the tropical Pacific ocean-atmosphere system, consisting of an OGCM and a simplified atmospheric model, whose forcing fields to the ocean include three components: wind stress, freshwater flux and heat flux (See Zhang and Busalacchi (2009) for more details). An empirical model for interannual variability of the penetration depth of solar radiation (H_p), derived from the ocean color data, is also explicitly included to represent the OBF.

Figure 2c exhibits one example of the H_p anomalies calculated using the empirical H_p model from the given SST anomalies (Fig. 2a). The model captures the large-scale interannual H_p variability during the ENSO evolution. However, as compared with the original field (Fig. 2b), the amplitude is systematically underestimated by a factor of about 2. Since some variance is always lost inevitably due to only some limited SVD modes retained in the empirical model, an amplification factor (α_{Hp}) is introduced to rescale its amplitude back to match what is derived from the ocean color data (Fig. 2b).

Note that the SST and H_p fields used for computing the SVD modes-based model are varying at the interannual timescale only, and the derived model is for estimating interannual H_p anomalies in the tropical Pacific associated with ENSO. Our previous efforts along these lines specified H_p in an uncoupled manner with physical parameters (*e.g.*, Murtugudde *et al.* 2002 and Ballabrera-Poy *et al.* 2007). Here H_p is a physical state-dependent parameter that allows for a feedback from ocean biology to the climate system and their active interactions during ENSO cycles, an approach taken by Timmermann and Jin (2002) to examine the ocean biology effect on climate.

(3) The hybrid coupled ocean-atmosphere model

A hybrid coupled model (HCM) for the tropical Pacific ocean-atmosphere system has been developed at ESSIC (Zhang *et al.* 2006). Fig. 3 illustrates a schematic for the HCM. Its ocean general circulation model (OGCM) is a primitive equation, sigma coordinate model whose details can be found in Murtugudde *et al.* (2002). The OGCM domain covers the tropical Pacific basin from 25°S to 25°N and from 124°E to 76°W, with the horizontal resolution of 1° in longitude and 0.5° in latitude, and 31 layers in the vertical. The atmospheric wind stress anomaly (τ_{inter}) model is also constructed empirically from the SVD analysis,

specifically relating τ_{inter} variability to large-scale SST anomalies (SST_{inter}). The attenuation depth of solar radiation (H_p) in the upper ocean is written as $H_p = H_p + \alpha_{Hp} \bullet H'_p$, consisting of the prescribed climatological part (H_p) and its interannual part (H'_p). The former is prescribed from a long-term annual mean field (Ballabrera-Poy et al. 2007) and the latter is calculated from the SST_{inter} anomalies. A scalar parameter, α_{Hp}, is introduced to represent the OBF strength. More recently, anomalous freshwater flux forcing has been also included in the HCM to take into account the freshwater flux-induced positive feedback in the tropical Pacific climate system (Zhang and Busalacchi 2009b).

3. Impacts of the OBF on interannual variability in the HCM

A control HCM run was performed in which interannual H_p variability is not allowed to feedback to SST in the HCM. As shown in Zhang and Busalacchi (2009b), the model can simulate interannual oscillations well. Next, we perform a series of runs in which the H_p-SST relationship derived from satellite data is included to take into account the OBF and interactions between ocean biology and physics (Fig. 4), with all the other model settings exactly the same as the control run. Note that the seasonally varying SST climatology (SST_{clim}) fields specified to compute large-scale SST_{inter} anomalies are all the same, which are determined from the forced OGCM climatological simulations.

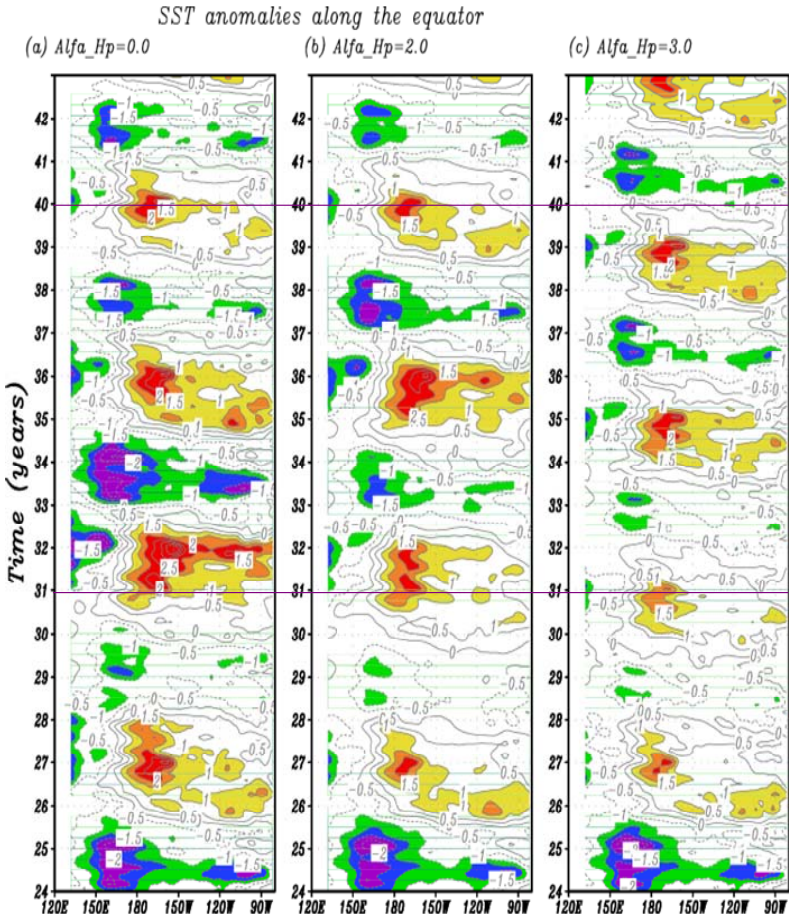

Fig. 4 Interannual H_p experiments: the longitude-time sections of SST anomalies along the equator simulated from the HCM with α_{Hp} =0.0 (a), α_{Hp} =2.0 (b), and α_{Hp} =3.0 (c). The contour interval is 0.5 °C. See Zhang et al. (2009) for more details.

Varying values of α_{Hp}, representing the OBF strength, are tested to investigate its effect on interannual variability. Simulations with α_{Hp}=0.0 are analyzed in Zhang and Busalacchi (2009b). One example of simulated SST anomaly fields is shown in Fig. 4 for two feedback runs with α_{Hp}=2.0 and α_{Hp}=3.0, respectively.

A striking feature is that the coupled models depict a pronounced interannual oscillation, with a dominant standing pattern of SST variability on the equator. As is well understood, the positive feedback associated with the wind-SST-thermocline coupling sustains interannual variability in the coupled system. When the OBF is taken into account, the effects can be clearly seen on the amplitude and oscillation periods of interannual variability (Fig. 4). The SST anomalies are weaker in the OBF runs, and become even weaker as the OBF is intensified. Moreover, runs with the OBF explicitly included exhibit clear phase differences as well. For example, a phase lead starts to show up clearly in year 30 due to an earlier transition from the warm to cold phases in the α_{Hp}=3.0 run. As such, the inclusion of the OBF causes a clear change in the oscillation periods. This can be more clearly seen in the power spectra estimated from the Niño3 SST indices (figures not shown): the interannual variability has a sharp peak at 4.2 years in the α_{Hp}=2.0 run, but has shifted

toward higher frequency band in the α_{Hp}=3.0 run, with two enhanced power peaks at 4.2 years and at 3.6 years, respectively. These results indicate that the ocean biology induced feedback effects tend to shorten the persistent time scales of SST anomalies. In addition, the irregularity is evidently large in the no and weak OBF runs (e.g., the year 32 in Fig. 4), but is significantly reduced in the $\boldsymbol{\alpha}_{Hp}$ =3.0 run due to the damping OBF effects on the system. Also, there is a change in the annual phasing of ENSO events, especially the peak season shifting from winter to summer. Some of these effects are not seen in Timmermann and Jin (2002) who used a simpler coupled model and a simpler formulation of the feedback.

The effects can be further quantified. The standard deviation (std) of Niño3 (Niño4) SST anomalies is 0.76°C (0.85°C) in the control run (α_{Hp}=0.0); it is reduced to 0.65°C (0.78°C) in the α_{Hp}=2.0 run, and to 0.59°C (0.69°C) in the α_{Hp}=3 run, respectively. Relative to the control run, these values represent a decrease of the amplitude by 14% (8%) in the α_{Hp}=2.0 run and by 22% (19%) in the α_{Hp}=3.0 run. Also, the std of the zonal wind stress in the Niño4 region is 0.19 dyn cm^{-2} in the α_{Hp}=0.0 run; it decreases to 0.17 dyn cm^{-2} in the α_{Hp}=2.0 run (a reduction by 11%) and to 0.15 dyn cm^{-2} in the α_{Hp}=3.0 run (a reduction by 21%). Thus, a significant fraction of the SST and surface wind variability can be attributed to the OBF effect in our model simulations.

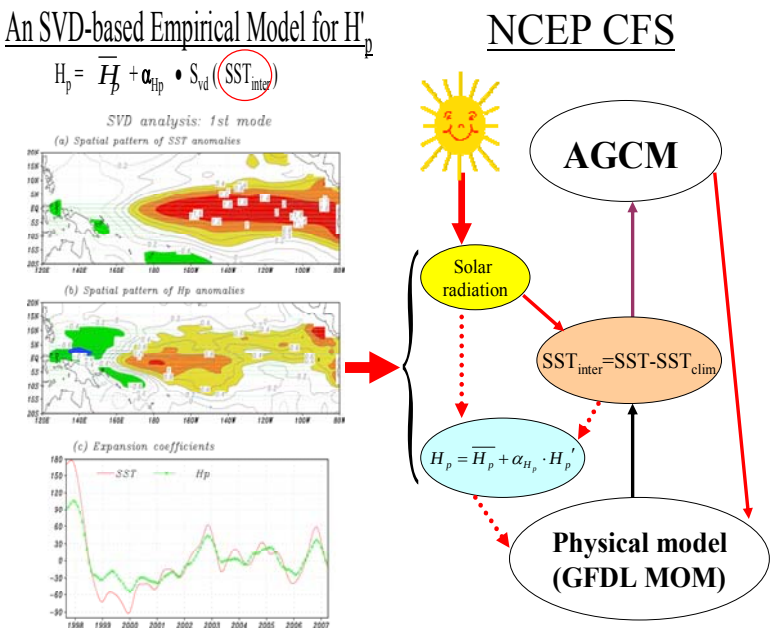

Fig. 5 A schematic illustrating the implementation of an empirical H_p model into the NCEP CFS to represent interannually varying ocean-biology-induced climate feedback for the tropical Pacific. Incoming solar radiation attenuates in the upper ocean due to pure water and due to biogenic components, which follows an exponential decline with depth. The effects of ocean biology-induced heating can be simply represented by the penetration depth of solar radiation in the upper ocean (H_p), a field linking the climate system to the marine ecosystem. H_p can be written as: $H_p = \overline{H_p} + \alpha_{Hp} \bullet H_p'$, which consists of a prescribed climatological part ($\overline{H_p}$) and its interannual part (H_p'). A scalar parameter, α_{Hp}, is introduced to represent the strength of ocean biology-induced feedback (OBF).

An empirical model for H'_p has been constructed using an SVD analysis technique from historical ocean color data during the periods Sep. 1997-Apr. 2007 (Zhang et al. 2010). Shown on the left are the spatial patterns for the first pair of singular vector of SST (a) and H_p (b) derived from the SVD analysis, and the time series associated with the first SVD mode (c), respectively. The spatial patterns of the SVD modes are used to construct an empirical model to parameterize interannual H_p variability. Then, a given SST anomaly can be converted to an H_p anomaly, which can be used to represent the effects on the penetrative solar radiation in the upper ocean of the CFS.

A heat budget analysis has been preformed to understand processes by which the OBF is affecting interannual variability. When the OBF is included, the induced feedback acts to reduce the cooling effect of the vertical mixing and entrainment during La Niña (*i.e.*, less cooling), but increase their cooling effect during El Niño (*i.e.*, less warming). This indicates that the inclusion of the OBF effects acts to counteract the positive SST-wind-thermocline feedback, leading to a weakening SST variability during ENSO cycles.

These results can be explained in terms of a negative feedback between ocean biology and climate system as follows. ENSO cycles are characterized by SST anomalies over the equatorial regions, which induce a biological response, as represented by large interannual H_p variability. During La Niña when SSTs are low in

the eastern and central tropical Pacific, H_p is negative and the solar radiation attenuates with depth strongly in the vertical. More solar heating is thus trapped in the mixed layer (ML), with less penetration downward into the subsurface. The direct effects are to add the solar heating more in the surface layer but less in the subsurface layers. The induced differential solar heating in the vertical acts to enhance the stratification and thus stabilize the upper ocean, with reduced mixing and entrainment of subsurface waters. These oceanic processes tend to weaken the cold SST anomalies generated by La Niña, with the wind-feedbacks favoring further reduction in upwelling and SST cooling. The effects on El Niño can be also seen but with opposite sense. As a result, the inclusion of the OBF in the HCM induces additional oceanic processes that act to counteract the positive SST-wind-thermocline feedback, thus reducing the strength of interannual variability.

4. An application to the NCEP CFS

At present, ocean models have considerable difficulty in representing biogeochemical processes. For example, current comprehensive ocean biogeochemistry models still can not realistically depict interannual H_p anomalies during ENSO cycles. Indeed, capturing the ocean biology-related H_p responses to physical anomalies requires realistic parameterizations of relevant physical and biogeochemistry processes both in the ocean, which are difficult to achieve at present. As a result, the bio-effects have not been included in coupled models currently used for real-time ENSO predictions. Due to the large amplitude and the demonstrated significant ocean biology-induced climate effects (*e.g.*, Zhang *et al.* 2009), interannual H_p anomalies are expected to have roles in modulating the mean climate and ENSO in the coupled atmosphere-ocean system of the tropical Pacific.

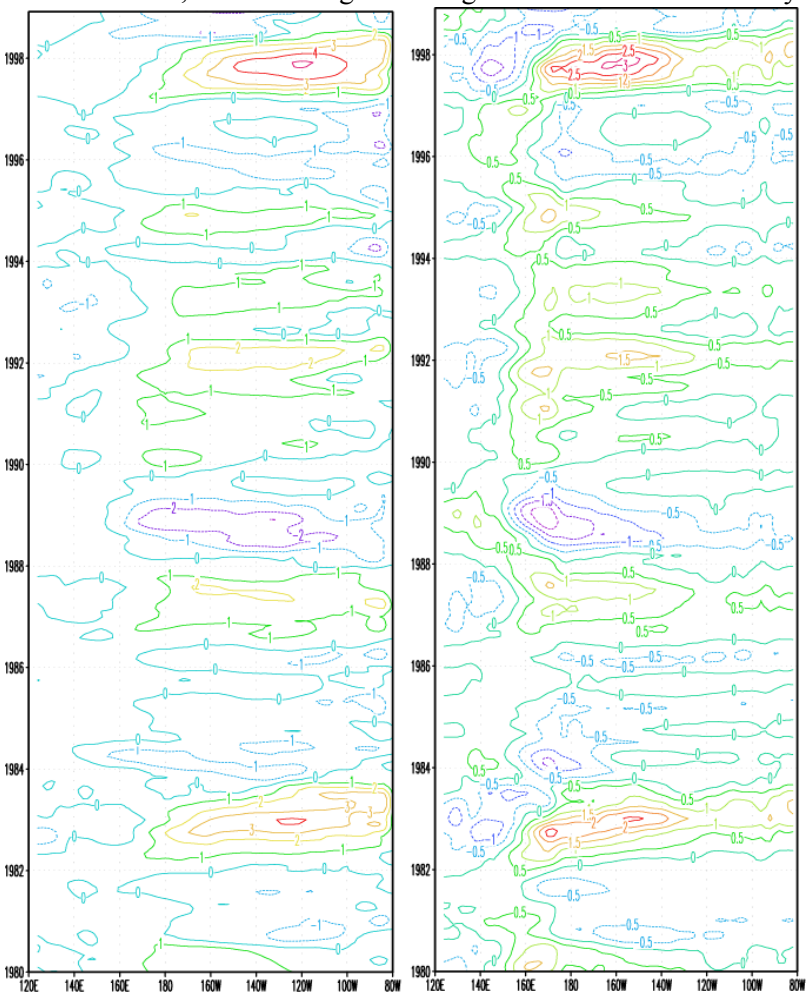

Fig. 6 Interannual SST (left) and H_p (right) anomalies along the equator simulated from the GFDL MOM3 (1/3°x1° in tropics, 1°x1° in extratropics, 40 layers), forced by observed atmospheric data (see Zhang et al. 2001). The H_p variability is obtained by using the empirical H_p model from the corresponding SST anomalies. The contour interval is 1°C for SST and 0.5 m for H_p.

Currently, the NCEP CFS has not taken into account biological components to represent the bio-feedback to the physical system (*e.g.*, Wang *et al.* 2005; Saha *et al.* 2006). It is very unlikely that in the near-term the CFS will include a comprehensive ocean biogeochemical model to resolve interannual H_p variability (In its recent release, the GFDL MOM 4 has the capability to handle geographically varying penetrating radiation; that is, a fixed chlorophyll climatology and H_p is specified without accounting for interannually varying effects). Therefore, ocean biology-induced feedbacks from the marine ecosystem to the physical system and the corresponding bio-climate coupling are missing (*e.g.*, Behringer 2007). The demonstrated interannual H_p effects on the large-scale mean state and seasonal-to-interannual climate variability have not been taken into account. As a result, the roles of ocean biology in tropical biases and

ENSO modulation are not known; the potential for improving ENSO simulation and prediction has not been explored.

Apparently, the missing bio-climate coupling in the NCEP CFS may well be a problem. Considering the lack of realistic H_p representations in the state-of-the-art NCEP CFS and considering the potential role of ocean biology in modulating mean climate and ENSO, we deem it important to include and understand the bio-effects in the CFS. Clearly, a key to addressing all these problems is how to realistically capture interannual H_p variability associated with ENSO.

The derived empirical H_p model can be embedded into the NCEP CFS to parameterize ocean biology-induced heating effects on the penetrative solar radiation in the upper ocean, making a direct contribution to the improvement in its oceanic component (Fig. 5). For example, the empirical H_p model derived using the SVD analysis technique has been tested to calculate an H_p response to interannual SST variability from an output of the GFDL OGCM simulation (Zhang *et al.* 2001). The OGCM is the version 3 of the GFDL MOM (Pacanowski and Griffies 1998), a finite-difference treatment of the primitive equations of motion using the Boussinesq and hydrostatic approximations in spherical coordinates. The vertical mixing scheme is the nonlocal K-profile parameterization of Large *et al.* (1999). The domain is that of the Pacific Ocean between 60°S and 65°N (Zhang *et al.* 2001; Zhang and Zebiak, 2002, 2003, 2004). The zonal resolution is 1.0°; the meridional grid spacing is 1/3° between 10°S and 10°N, gradually increasing to 1.0° at 30°N and 30°S and fixed at 1.0° in the extratropics; there are 40 levels in the vertical, with 17 levels in the upper 450 m, forced by prescribed atmospheric data during the periods 1949-2000. Interannual SST anomalies along the equator simulated are shown in Fig. 6a . The interannual H_p variability is obtained by using the empirical $H_p^{97\text{-}07}$ model from the corresponding SST anomalies. Using the simulated interannual SST anomalies as an input to the empirical H_p model, interannual H_p anomalies can be estimated (Fig. 6b). Large H_p anomalies and coherent H_p–SST relationships are evident in association with ENSO. The effects on the penetrative solar radiation are expected in the ocean simulation. Further modeling experiments are underway to investigate the impacts of ocean biology on large-scale mean climate and its variability and predictability in the tropical Pacific. In particular, the benefits for ENSO simulation and prediction will be quantified. As demonstrated in the hybrid modeling study (Zhang *et al.* 2009), ocean biology in the tropical Pacific is expected to contribute to the modulation of the mean climate and ENSO through the penetrative effect on solar radiation, leading to an improved climate forecast in the NCEP CFS.

References

Anderson W. G., A. Gnanadesikan, R. Hallberg, J. Dunne, B. L. Samuels, 2007: Impact of ocean color on the maintenance of the Pacific cold tongue. *Geophys. Res. Lett.*, **34**, L11609, doi:10.1029/2007GL030100.

Ballabrera-Poy J., R. G. Murtugudde, J. R. Christian, A. J. Busalacchi, 2003: Signal-to-noise ratios of observed monthly tropical ocean color, *Geophys. Res. Lett.*, **30**, 1645, doi:10.1029/2003GL016995.

Ballabrera-Poy, J., R. G. Murtugudde, R.-H. Zhang, and A. J. Busalacchi, 2007. Coupled ocean-atmosphere response to seasonal modulation of ocean color: Impact on interannual climate simulations in the tropical Pacific. *J. Climate*, **20**, 353-374.

Behringer, D. W. (2007), The Global Ocean Data Assimilation System at NCEP, paper presented at the 11th Symposium on Integrated Observing and Assimilation Systems for Atmosphere, Oceans, and Land Surface, Am. Meteorol. Soc., San Antonio, Tex.

Chavez, F., P. Strutton, and M. McPhaden: 1998: Biological-physical coupling in the central equatorial Pacific during the onset of the 1997-98 El Niño. *Geophys. Res. Lett.*, **25**(19), 3543-3546.

Chavez, F. P., P. G. Strutton, G. E. Friedrich, R. A. Feely, G. C. Feldman, D. G. Foley, M. J. McPhaden , 1999: Biological and chemical response of the equatorial Pacific ocean to the 1997–98 El Niño. *Science*. **286**, 2126–2131.

Large, W. G., and P. R. Gent, 1999: Validation of vertical mixing in an equatorial ocean model using large eddy simulations and observations. *J. Phys. Oceanogr*., **29**, 449-464.

Lengaigne, M. , C. Menkes, O. Aumont, T. Gorgues, L. Bopp, J.-M. André and G. Madec, 2007: Influence of the oceanic biology on the tropical Pacific climate in a coupled general circulation model. *Clim. Dyn.,* **28**, 503-516.

Lewis, M. R., M. E. Carr, G. C. Feldman, W. Esias, C. McClain, 1990: Influence of penetrating solar radiation on the heat budget of the equatorial Pacific. *Nature*, **347**, 543–546.

Manizza, M., C. Le Quéré, A. J. Watson, and E. T. Buitenhuis, 2005: Bio-optical feedbacks among phytoplankton, upper ocean physics and sea-ice in a global model. *Geophys. Res. Lett.*, **32**, L05603, doi:10.1029/2004GL020778.

Marzeion, B., A. Timmermann, R. Murtugudde, and F.-F. Jin, 2005: Biophysical feedbacks in the tropical Pacific. *J. Climate*, **18**, 58–70.

McClain, C. R., M. L. Cleave , G. C. Feldman, W. W. Gregg, S. B. Hooker , N. Kuring, 1998: Science quality SeaWiFS data for global biosphere research. *Sea Technol*, **39**, 10–16

Murtugudde, R., J. Beauchamp, C. R. McClain, M. Lewis, and A. J. Busalacchi, 2002: Effects of penetrative radiation on the upper tropical ocean circulation. *J. Climate*, **15**, 470-486.

Nakamoto, S., S. Kumar, J. Oberhuber, J. Ishizaka, K. Muneyama, and R. Frouin, 2001: Response of the equatorial Pacific to chlorophyll pigment in a mixed layer isopycnal ocean general circulation model, *Geophys. Res. Lett.,* **28**(10), 2021-2024.

Pacanowski, R. C., and S. M. Griffies, 1998: *MOM 3.0 Manual*, NOAA/Geophysical Fluid Dynamics Laboratory, 700 pp.

Paulson, C. A., and J. J. Simpson, 1977: Irradiance measurements in the upper ocean. *J. Phys. Oceanogr*. **7**, 952–956.

Saha, S., S. Nadiga, C. Thiaw, J. Wang, W. Wang, Q. Zhang, H. M. Van den Dool, H.-L. Pan, S. Moorthi, D. Behringer, D. Stokes, M. Peña, S. Lord, G. White, W. Ebisuzaki, P. Peng, and P. Xieet al., 2006: The NCEP climate forecast system, *J. Climate*, **19**, 3483-3517.

Strutton, P. G. and F. P. Chavez, 2004: Biological heating in the equatorial Pacific: Observed variability and potential for real-time calculation. *J. Climate*, **17**, 1097–1109.

Timmermann A. and F.-F. Jin, 2002: Phytoplankton influences on tropical climate. *Geophys. Res. Lett.*, **29**, 2104, doi:10.1029/2002GL015434.

Wang, W., S. Saha, H.-L. Pan, S.Nadiga, and G. White, 2005: Simulation of ENSO in the new NCEP Coupled Forecast System Model (CFS). Mon. Wea. Rev, 133, 1574–1593.

Wetzel, P., E. Maier-Reimer, M. Botzet, J. Jungclaus, N. Keenlyside, and M. Latif, 2006: Effects of ocean biology on the penetrative radiation in a coupled climate model. *J. Climate*, **19**, 3973–3987.

Zhang, R.-H., T. Kagimoto, and S. E. Zebiak, 2001: Subduction of decadal North Pacific thermal anomalies in an ocean GCM, *Geophys. Res. Lett.,* **28**, 2449-2452.

Zhang, R.-H., and S. E. Zebiak, 2002: Effect of penetrating momentum flux over the surface mixed layer in a z-coordinate OGCM of the tropical Pacific. *J. Phys. Oceanogr.*, **32**, 3616-3637.

Zhang, R.-H., and S. E. Zebiak, 2003: Embedding a SST anomaly model into a z-coordinate oceanic GCM for producing El Nino oscillation in the tropical Pacific climate system. *Geophys. Res. Lett*., Vol. **30**, No. 4, 1176, doi:10.1029/2002GL015428.

Zhang, R.-H., and S. E. Zebiak, 2004: An embedding method for improving interannual variability simulations in a hybrid coupled model of the tropical Pacific ocean-atmosphere system. *J. Climate,* **17**, 2794-2812.

Zhang, R.-H., A. J. Busalacchi, and R. G. Murtugudde, 2006: Improving SST anomaly simulations in a layer ocean model with an embedded entrainment temperature submodel. *J. Climate,* **19**, 4638–4663.

Zhang, R.-H., and A. J. Busalacchi, 2009a: An empirical model for surface wind stress response to SST forcing induced by tropical instability waves (TIWs) in the eastern equatorial Pacific. *Mon. Wea. Rev*., **137**, 2021–2046.

Zhang, R.-H., and A. J. Busalacchi, 2009b: Freshwater flux (FWF)-induced oceanic feedback in a hybrid coupled model of the tropical Pacific. *J. Climate*, **22**, No. 4, 853–879.

Zhang, R.-H., A. J. Busalacchi, X. Wang, J. Ballabrera-Poy, R. G. Murtugudde, E. C. Hackert, and D. Chen, 2009: Role of ocean biology-induced climate feedback in the modulation of El Niño-Southern Oscillation, *Geophys. Res. Lett.*, 36, L03608, doi:10.1029/2008GL036568.

Zhang, R.-H., A. J. Busalacchi, Dake Chen and Guihua Wang, 2010: Using satellite ocean color data to derive an empirical model for the penetration depth of solar radiation (H_p) in the tropical Pacific ocean, *J. Geophys. Res.*, accepted.

US National Oceanic and Atmospheric Administration
Climate Test Bed Joint Seminar Series
NCEP, Camp Springs, Maryland, 3 February 2010

ENSO Prediction Skill in the NCEP CFS

Renguang Wu[1], Ben P. Kirtman[1,2] and Huug van den Dool[3]

[1]*Center for Ocean-Land-Atmosphere Studies, Calverton, Maryland*
[2]*Rosenstiel School of Marine and Atmospheric Science, University of Miami, Miami, FL*
[3]*Climate Prediction Center, National Centers for Environmental Prediction, Camp Springs, MD*

1. Introduction

A well-known feature in ENSO forecasts is a significant drop in prediction skill during boreal spring (Kirtman *et al.* 2001), particularly in terms of eastern Pacific SST correlation coefficients. This spring prediction barrier has been attributed to the low variance of NINO3 SST anomalies in boreal spring (Xue *et al.* 1994; Torrence and Webster 1998; Clarke and Van Gorder 1999). In the spring season, the Walker circulation is weak and the east-west sea level pressure and SST gradient along the equatorial Pacific is at a minimum (Webster and Yang 1992; Webster 1995; Lau and Yang 1996). Under such conditions, the initial errors and "weather" noise in the models can project strongly onto ENSO modes, leading to large error growth and deteriorating the forecasts. Chen *et al.* (1995) suggested that the spring predictability barrier is not intrinsic to the real climate system and that it may be a problem of the models. Jin and Kinter (2009) indicated that systematic model errors are major factors limiting the predictability and degrading the forecast skill.

One important factor for the eastern equatorial SST anomalies is the equatorial Pacific thermocline change. Thus, it may be asked whether there is a similar prediction barrier in the thermocline. Indeed, a boreal winter prediction barrier was identified in the equatorial Pacific heat content (Balmaseda *et al.* 1995). In analogy with low NINO3 SST variance in boreal spring, the equatorial Pacific warm water volume anomalies tend to have small variance in boreal winter (McPhaden 2003). Since equatorial Pacific heat content fluctuations are closely related to surface wind changes in the western equatorial Pacific (Kirtman 1997; Weisberg and Wang 1997; Mayer and Weisberg 1998; Wang *et al.* 1999), is there an associated barrier for the low level winds in that area?

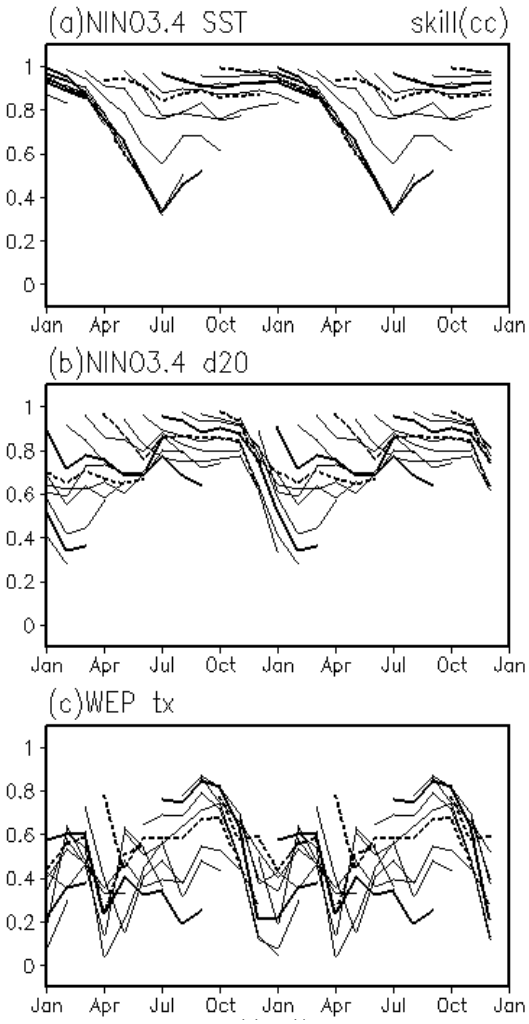

Fig. 1 Correlation skill of NINO3.4 SST (a), NINO3.4 thermocline depth (b), and western equatorial Pacific zonal wind stress (c) derived from CFS ensemble mean forecasts. For clarity of presentation two repeating years are shown.

The NCEP CFS (Saha *et al.* 2006) has become an important forecast tool. Because of the large impacts of ENSO on climate fluctuations in both the tropics and extratropics, it is important to understand how the CFS performs in terms of tropical Pacific SST forecasts. Saha et al. (2006) have shown that the CFS SST forecasts experience a large drop in skill in boreal spring. What are the plausible reasons for the drop in skill? Is it due to the effects of noise or related to the reduction of signal-to-noise ratio (Torrence and Webster 1998)? Understanding these questions would help toward a better

Correspondence to: Renguang Wu, Center for Ocean-Land-Atmosphere Studies, 4041 Powder Mill Road, Suite 302, Calverton, MD 20705; E-mail: renguang@cola.iges.org

application of ENSO forecasts made based on the CFS. The present study addresses these questions based on the NCEP CFS 24-year retrospective ensemble forecasts.

2. The prediction barrier

Here, the prediction skill is measured by the correlation coefficient between the CFS ensemble mean forecasts and observations. The prediction skill is calculated based on area-mean anomalies. Figure 1 shows the prediction skills for the NINO3.4 (5°S-5°N, 170°-120°W) SST, NINO3.4 thermocline depth, and the western equatorial Pacific (5°S-5°N, 130°-170°E) zonal wind stress.

The NINO3.4 SST forecast skill has an apparent drop during April-June for forecasts starting before March (Fig. 1a). The lowest forecast skill (less than 0.4) appears in July for forecasts starting from November-January. For forecasts starting after March, the drop in skill is much less with correlations maintained at a high level during November-February. These results are consistent with Saha *et al.* (2006), and with reported skill by many other methods as well (see Kirtman *et al.* 2001).

The NINO3.4 thermocline depth experiences an obvious drop in the forecast skill as well. The deterioration of skill is seen during December-February with the lowest forecast skill appearing in February-March (Fig. 1b), leading the drop in skill in the NINO3.4 SST by about 4-5 months. The time difference of the drop in skill between the NINO3.4 SST and thermocline depth is consistent with their phase lag as shown in previous studies (Zebiak and Cane 1987; Balmaseda *et al.* 1995). This suggests that the changes in the forecast skill for these two quantities are related.

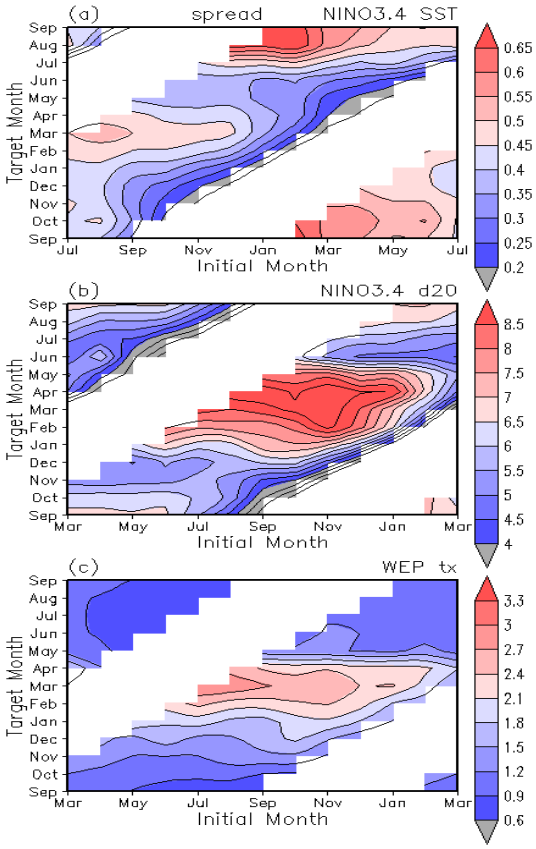

Fig. 2 Ensemble spread for monthly mean NINO3.4 SST (a), NINO3.4 thermocline depth (b), and western equatorial Pacific zonal wind stress (c) derived from CFS forecasts.

The western equatorial Pacific zonal wind stress shows generally lower skill compared to the NINO3.4 SST and thermocline depth. There are three periods during which the forecast skill for the wind stress displays obvious drops. The first and most pronounced one is during October-December (Fig. 1c). This one leads the drop in skill in the NINO3.4 thermocline depth by about 1-2 months. In view of the phase relationship between the western equatorial Pacific wind stress and equatorial Pacific thermocline changes in the ENSO evolution (Wang *et al.* 1999), this drop in skill in the wind stress is likely related to that in the thermocline depth. The second drop in skill is seen in March-April, which is likely related to the effects of atmospheric noise. Another drop in skill is seen in July-August. Compared to the other two, this latter drop in skill is relatively weak and is only seen for some of the forecasts.

Previous studies have focused on the substantial decrease in observation-prediction correlation in the NINO3 SST or the SO index across the boreal spring and have attributed the spring prediction barrier to the maximum error growth in boreal spring (*e.g.*, Webster 1995). The forecast skill in Fig. 1 shows that the drop in skill in NINO3.4 thermocline depth and western equatorial Pacific surface wind stress precedes the drop in skill in NINO3.4 SST in boreal spring. This phase relationship suggests that the prediction barrier could be an intrinsic feature of the coupled model (i.e., coupled model error), although the noise may also play a role.

3. Possible reasons for the prediction barrier

If the noise is critical to the low skill, then we would expect to see large noise when the skill drops. To examine, whether this is so, we show in Fig. 2 the ensemble spread for the NINO3.4 SST, NINO3.4

thermocline depth, and the western equatorial Pacific zonal wind stress. Here, the ensemble spread is used as a proxy for noise.

For the NINO3.4 SST, the largest spread is seen around August-September (Fig. 2a) when the eastern equatorial Pacific cold tongue is the coldest and the SST front surrounding the cold tongue is the strongest. The spread is small around May when the skill drops quickly. For the NINO3.4 thermocline depth, the largest spread is seen around March-April for most of the forecasts (Fig. 2b). Around December when the skill drop, the spread is small. For the western equatorial Pacific zonal wind stress, the largest spread is around March (Fig. 2c), which coincides with the secondary skill drop. The main skill drop around November is in a period when the spread increases. The temporal relationship between the seasonal change of the prediction skill and the spread indicates that the prediction barrier is unlikely to be explained by the noise variation.

To further demonstrate whether the noise contributes to the drop in the prediction skill, we show in Fig. 3 the correlation skill of three quantities calculated using the "perfect model approach" based on the 15-member forecasts. In this calculation, one member of the forecasts is treated as "observation" and the ensemble mean of the other 14 members is treated as "forecast". The correlation is calculated for each of the 15 members alternatively treated as "observation" and Fig. 3 shows the mean of the 15 correlations calculated for NINO3.4 SST, NINO3.4 thermocline depth, and the western equatorial Pacific zonal wind stress. Under the perfect model assumption, the model systematic errors do not exist and thus the change in the correlation skill is attributed to the impacts of noise and initial condition errors. Comparison of Fig. 3 and Fig. 1 illustrates whether noise contributes to the prediction skill and to what extent.

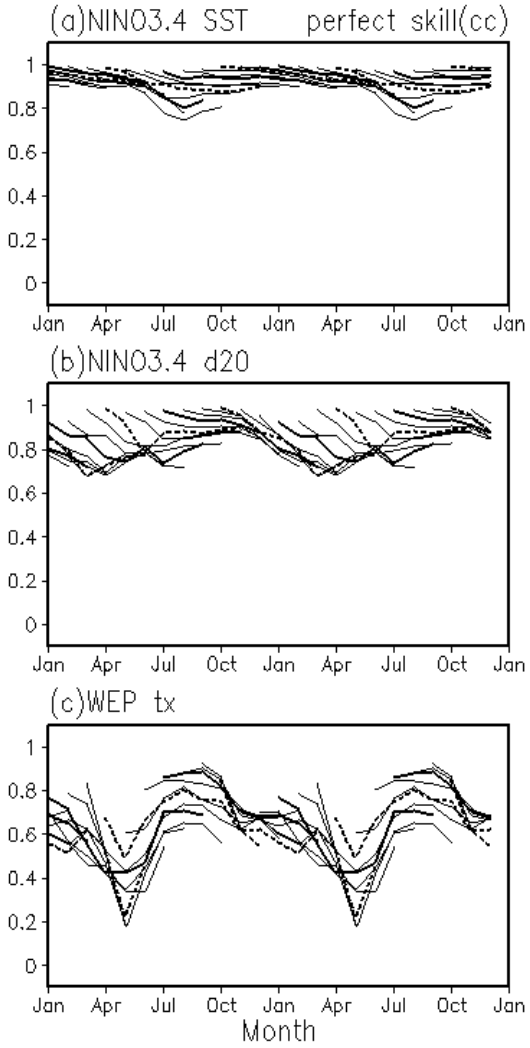

Fig. 3 Correlation skill of NINO3.4 SST (a), NINO3.4 thermocline depth (b), and western equatorial Pacific zonal wind stress (c) calculated using the perfect model approach from CFS forecasts.

For NINO3.4 SST, the lowest predictability is seen during July-September (Fig. 3a), consistent with Saha *et al.* (2006, their Fig.3). The drop in skill, however, is only about 0.2, much less than that seen in Fig. 1a. In addition, the timing of the drop in skill is later than that seen in Fig. 1a. For NINO3.4 thermocline depth, the drop in skill is larger compared to NINO3.4 SST. The lowest skill is about 0.7 during March-April (Fig. 3b). The low skill in the thermocline depth leads that in the SST by about 4-5 months. For some of the forecasts, there is a secondary correlation minimum in July. Compared to the skill in Fig. 1b, the drop in skill is much less and occurs at a later time. For the western equatorial Pacific zonal wind stress, the drop in skill is more pronounced, with the lowest correlations occurring around May (Fig. 3c). The drop in skill during March-April seems to occur at the same time as the one of the drops seen in Fig 1c.

The above relationship indicates that the noise does not entirely explain the drops in the prediction skill seen in the CFS ensemble forecasts. The question then is, what is responsible for the decline in the prediction skill? Our analyses suggest that the CFS atmospheric wind response to SST anomalies is significantly different from observations, and that this difference is amplified by coupled feedback, ultimately leading to the spring prediction barrier. This is demonstrated in the following.

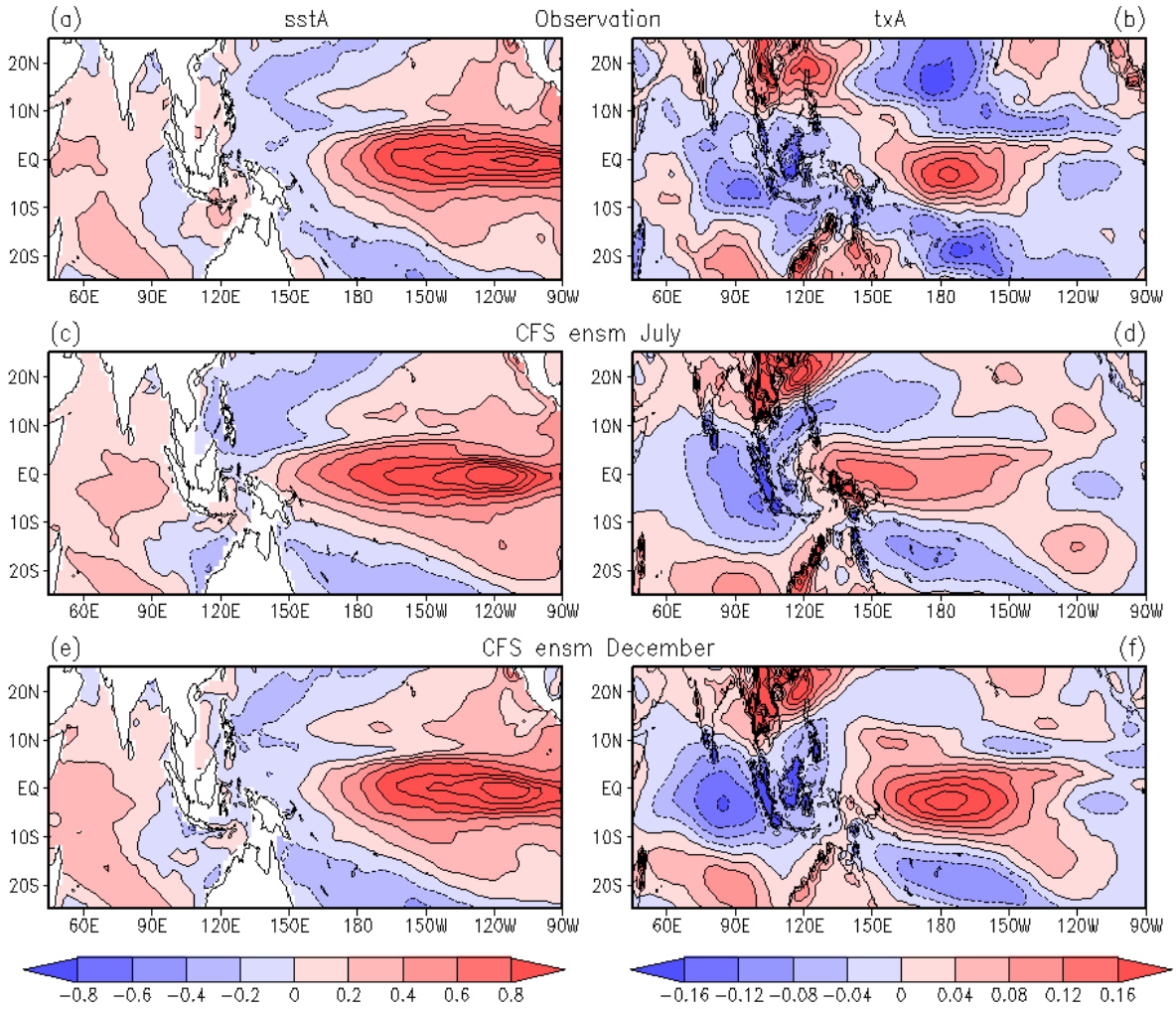

Fig. 4 Anomalies of December SST (°C) (a, c, e) and zonal wind stress (dyn/cm^2) (b, d, f) obtained as regression on December NINO3.4 SST. (a)-(b) are derived from observations, (c)-(d) from CFS ensemble mean forecasts starting from July, (e)-(f) from CFS ensemble mean forecasts starting from December. The contour interval is 0.2°C for SST and 0.04 dyn/cm^2 for wind stress.

Figure 4 shows the December SST and surface zonal wind stress anomalies obtained by regression onto the December NINO3.4 SST for observations, the CFS forecasts from July and December. For the forecasts initialized in December, the SST anomalies in the tropical Indo-Pacific Ocean (Fig. 4e) are in good agreement with the observational estimates (Fig. 4a). The zonal wind stress, however, shows noticeable differences. The anomalous westerly winds over the equatorial central Pacific are larger in the CFS forecasts (Fig. 4f) than in observations (Fig. 4b). In addition, the westerly winds extend more westward in the forecasts compared to observations. For the forecasts starting from July, the westward extension of anomalous westerly winds is more obvious (Fig. 4d). This is accompanied by westward extension of positive SST anomalies (Fig. 4c).

The differences in the zonal wind stress can affect the ENSO phase transition through ocean-atmosphere coupled processes. Figure 5 shows the temporal evolution of NINO3.4 SST, NINO3.4 thermocline depth, NINO3.4 zonal wind stress, and western equatorial Pacific zonal wind stress from CFS forecasts starting from December and July and from observations, which are obtained by regression onto December NINO3.4 SST. For forecasts starting from December, the initial month (December) NINO3.4 SST anomalies are nearly the same in the forecasts and observations (Fig. 5a). The westerly wind stress anomalies, however, are very different. Compared to observations, anomalous westerlies in the NINO3.4 region are larger throughout the 9-month forecast period (Fig. 5d) and those in the western equatorial Pacific are larger in December (Fig. 5c).

The larger westerly anomalies favor the maintaining of positive thermocline depth anomalies in the NINO3.4 region for a longer period in the CFS forecasts than in observations (Fig. 5b). This leads to a longer persistence of positive SST anomalies in the NINO3.4 region (Fig. 5a) and, in turn, to westerly anomalies over the equatorial central Pacific (Fig. 5d). At the time when observed SST anomalies are near zero, the CFS forecasts still have about 0.5°C positive SST anomalies. As such, low correlation skill appears at the time of observed phase transition. Note that, in March and April, the CFS forecast western equatorial Pacific wind anomalies are easterly (Fig. 5c), which cannot be explained by SST anomalies in the central-eastern equatorial Pacific. This suggests the impacts of other factors.

The differences in the time of phase transition of western equatorial Pacific zonal wind stress and NINO3.4 thermocline depth anomalies are more clearly seen in the forecasts starting from July. For these forecasts, westerly wind anomalies in the western equatorial Pacific are large and remain so until February, whereas in observations the westerly anomalies start to decrease quickly around November and become small in February (Fig. 5g). The differences in the NINO3.4 zonal wind stress anomalies are small before December, but after that these anomalies are larger in the forecasts than in observations (Fig. 5h). Corresponding to these wind stress differences, the CFS forecasts maintain positive thermocline depth anomalies in the NINO3.4 region for a longer time, whereas in observations the thermocline depth anomalies become small after December (Fig. 5f). This seems to delay the weakening of positive SST anomalies in the NINO3.4 region in the forecasts compared to observations (Fig. 5e). The differences in SST anomalies, in turn, contribute to larger westerly anomalies, in particular, during December-February (Figs. 5g-h).

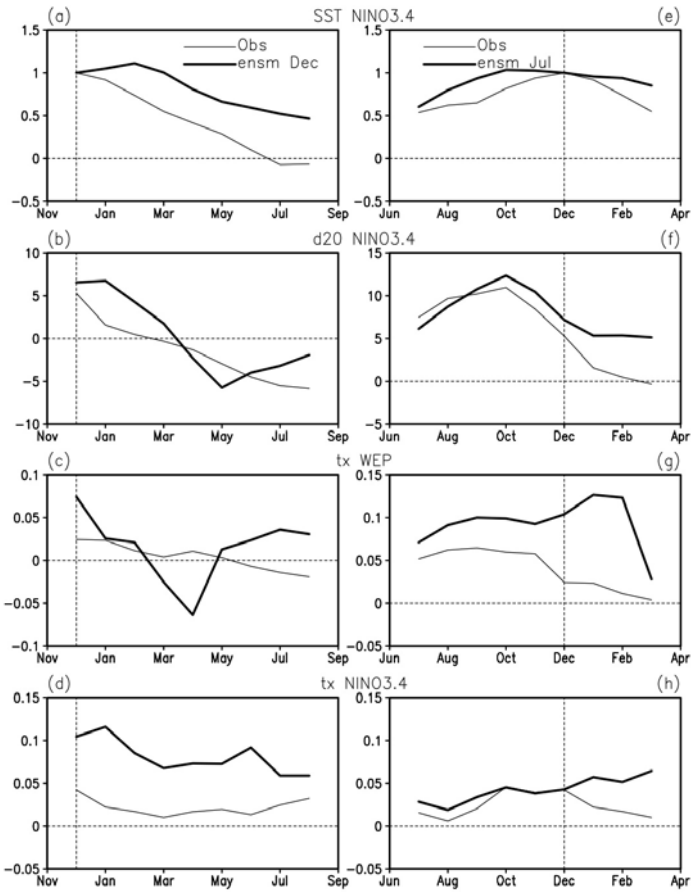

Fig. 5 Anomalies of NINO3.4 SST (°C) (a, e), NINO3.4 thermocline depth (m) (b, d), western equatorial Pacific zonal wind stress (dyn/cm^2) (c, g), and NINO3.4 zonal wind stress (dyn/cm^2) (d, h) obtained as regression on December NINO3.4 SST. (a)-(d) are from observations and CFS ensemble mean forecasts starting from December, (e)-(h) are the from observations and CFS ensemble mean forecasts starting from July. Thin curves are for observations and thick curves are for CFS ensemble mean forecasts.

4. Summary

The SST, thermocline depth, and surface wind stress over the equatorial Pacific are closely coupled. Model forecasts of ENSO have often encountered a reduced skill in boreal spring. The present study shows that the CFS retrospective forecasts experience a prominent drop in skill in boreal spring for NINO3.4 SST forecasts, in agreement with Saha *et al.* (2006), and this is preceded by a drop in skill in boreal winter in the NINO3.4 thermocline depth and western equatorial Pacific zonal wind stress.

The atmospheric noise has a large impact on the prediction skill of the zonal wind stress in boreal spring. However, its effects on the prediction skill in association with ENSO are relatively small with this model. The analysis presented here shows that in the CFS the atmospheric wind response to ENSO-related SST anomalies

is too strong and extends too westward. This deficiency seems to be amplified by coupled processes. As a result, the thermocline depth anomalies actually persist for too long and the ENSO phase transition is delayed in the CFS compared to observations. Our interpretation of this result is that the excessive persistence or delayed phase transition associated with wind stress structural errors is why CFS has a spring prediction barrier. Our results suggest that the spring prediction barrier is largely due to deficiencies in the models, in agreement with Chen *et al.* (1995) and Jin and Kinter (2009).

Previous studies have shown that the western equatorial Pacific zonal wind stress is an important element in the ENSO evolution (*e.g.*, Weisberg and Wang 1997; Wang *et al.* 1999). Not surprisingly, the present study indicates that the ENSO prediction skill is closely linked to the wind stress prediction skill. However, we also suggest that by improving the atmospheric model wind stress response to SST anomalies we can expect an improvement in ENSO forecast skill.

References

Balmaseda, M. A., M. K. Davey, and D. L. T. Anderson, 1995: Decadal and seasonal dependence of ENSO prediction skill. *J. Climate*, **8**, 2705-2715,

Chen, D., S. E. Zebiak, A. J. Busalacchi, and M. A. Cane, 1995: An improved procedure for El Niño forecasting. *Science*, **269**, 1699-1702.

Clarke, A. J., and S. Van Gorder, 1999: The connection between the boreal spring Southern Oscillation persistence barrier and biennial variability. *J. Climate*, **12**, 612-620.

Jin, E. K., and J. L. Kinter III, 2009: Characteristics of tropical Pacific SST predictability in coupled GCM forecasts using the NCEP CFS. *Clim. Dyn.*, 32, 675-691.

Kirtman, B. P., 1997: Oceanic Rossby wave dynamics and the ENSO period in a coupled model. *J. Climate*, **10**, 1690-1705.

Kirtman, B. P., J. Shukla, M. A. Balmaseda, N. E. Graham, C. Penland, Y. Xue, and S. E. Zebiak, 2001: Current status of ENSO forecast skill: A report to the Climate Variability and Predictability (CLIVAR) Numerical Experimentation Group (NEG), WCRP Informal Report No. 23/01, 31pp. [Available at http://www.clivar.org/publications/wg_reports/wgsip/nino3/report.htm]

Lau, K.-M., and S. Yang, 1996: The Asian monsoon and predictability of the tropical ocean-atmosphere system. *Quart. J. Roy. Meteorol. Soc.*, **122**, 945-957.

Mayer, D. A., and R. H. Weisberg, 1998: El Niño-Southern Oscillation-related ocean-atmosphere coupling in the western equatorial Pacific. *J. Geophys. Res.*, **103(C9)**, 18635-18648.

McPhaden, M. J., 2003: Tropical Pacific ocean heat content variations and ENSO persistence barrier. *Geophys. Res. Lett.*, **30**, 1480, doi:10.1029/2003GL016872.

Saha S., S. Nadigam C. Thiaw, J. Wang, W. Wang, Q. Zhang, H. M. van den Dool, H.-L. Pan, S. Moorthi, D. Dehringer, S. Stokes, M. Peña, S. Lord, G. White, W. Ebisuzaki, P. Peng, and P. Xie, 2006: The NCEP Climate Forecast System. *J. Climate*, **19**, 3483-3517.

Torrence, C., and P. J. Webster, 1998: The annual cycle of persistence in the El Niño/Southern Oscillation. *Quart. J. Roy. Meteorol. Soc.*, **124**, 1985-2004.

Wang, B., R. Wu, and R. Lukas, 1999: Roles of the western North Pacific wind variation in thermocline adjustment and ENSO phase transition. *J. Meteor. Soc. Japan*, **77**, 1-16.

Webster, P. J., and S. Yang, 1992: Monsoon and ENSO: Selectively interactive systems. *Quart. J. Roy. Meteorol. Soc.*, **118**, 877-926.

Webster, P. J., 1995: The annual cycle and predictability of the tropical coupled ocean-atmosphere system. *Meteorol. Atmos. Phys.*, **56**, 33-55.

Weisberg, R. H., and C. Wang, 1997: Slow variability in the equatorial west-central Pacific in relation to ENSO. *J. Climate*, **10**, 1998-2017.

Xue, Y., M. A. Cane, S. E. Zebiak, and M. B. Blumenthal, 1994: On the prediction of ENSO: A study with a low-order Markov model. *Tellus*, **46A**, 512-528.

Zebiak, S. E., and M. A. Cane, 1987: A model El Niño-Southern Oscillation. *Mon. Wea. Rev.*, **115**, 2262-2278.

US National Oceanic and Atmospheric Administration
Climate Test Bed Joint Seminar Series
IGES/COLA, Calverton, Maryland, 24 March 2010

Summer Season Precipitation Prediction over America with the NCEP Climate Forecast System Using Different Land Components and Different Sea Surface Temperatures

Rongqian Yang, Michael Ek, Jesse Meng and Ken Mitchell

Environmental Modeling Center, NOAA/NWS/NCEP
Camp Springs, MD, 20746

1. Introduction

Skillful short-term weather forecasts, which rely heavily on quality atmospheric initial conditions, have a fundamental limit of about two weeks (Lorenz, 1963) due to the chaotic nature of the atmosphere. Useful climate forecasts on seasonal time scales, on the other hand, require well-simulated large-scale atmospheric response to slowly varying lower boundary forcings from both ocean and land surface. The critical importance of ocean memory has been well recognized (*e.g.*, Shukla, 1998; Wallace *et al.*, 1998) whereby large-scale anomalies in the atmospheric general circulation on seasonally-averaged time scales are forced first and foremost by large-scale anomalies in sea surface temperature (SST), especially over the El-Niño and Southern Oscillation (ENSO) regions of the tropical Pacific Ocean. In contrast to SST anomalies, it has been proven notably more difficult to demonstrate that land surface anomalies (soil moisture, snowpack) have meaningful positive impact on continental seasonal forecast skill in coupled climate models. Past studies show that soil moisture anomalies can persist for months (Vinnikov *et al.*, 1996), and soil moisture feedback can have notable effects on precipitation and modify other quantities through surface evaporation and surface energy processes (*e.g.*, Shukla and Mintz, 1982; Koster and Suarez, 2001; Wu and Dickinson, 2004). The feedback was also found to vary with climate regimes (*e.g.*, Koster *et al.*, 2000; Zhang *et al.*, 2008). Past studies on such land-atmosphere feedback strongly indicate that careful treatment of soil moisture and its associated anomalies in coupled climate models is important to improving seasonal predictions.

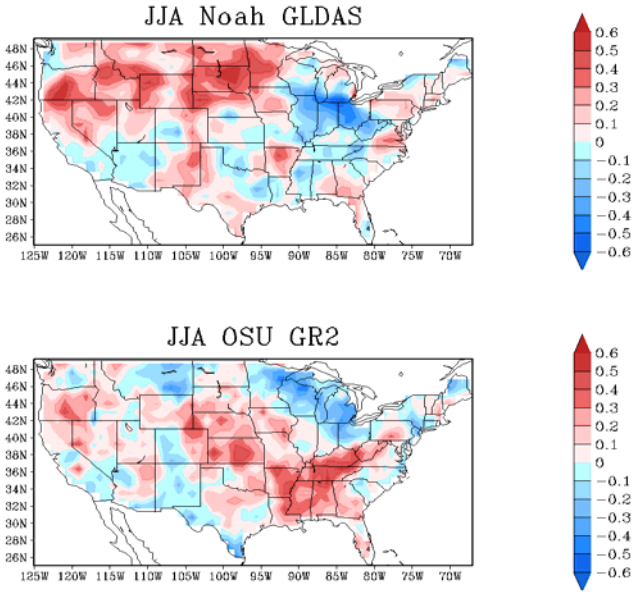

Fig. 1 Predicted JJA precipitation anomaly correlation over CONUS (25-year average).

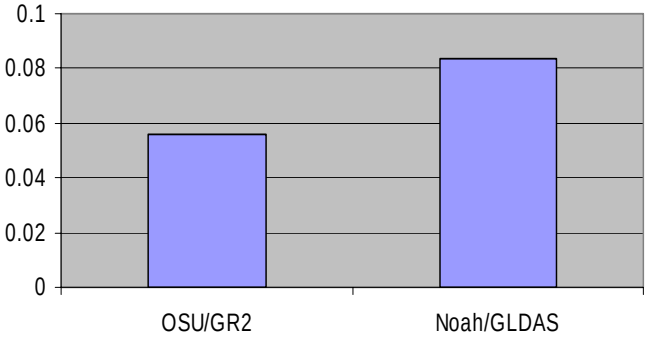

Fig. 2 CONUS-averaged predicted JJA precipitation anomaly correlation scores (25-year average).

Due to a paucity of global soil moisture observations and the complex nature of land-atmospheric interactions, land-anomaly forcing is more difficult than ocean-anomaly forcing to separate from the natural chaotic variability of seasonal circulations (*i.e.*, land-anomaly impact has a smaller signal to noise ratio than SST impact). Efforts to understand the linkage between land surface anomalies and the spawning of seasonal

Correspondence to: Rongqian Yang, Environmental Modeling Center, NOAA/NWS/NCEP, Camp Springs, MD, 20746;
E-mail: Rongqian.Yang@noaa.gov

atmospheric circulation anomalies have to rely on developing more advanced land surface models. A better representation of land physics in climate models becomes the first step toward understanding how much the land contributes to climate variations. The efforts to understand the complex land-atmosphere interactions are also compounded by the fact that the prediction results from a given General Circulation Model (GCM) are sensitive to how the land-component of the GCM is initialized and the starting dates used in the integrations (*e.g.*, Dirmeyer, 2001; Koster *et al.*, 2000, 2003, and 2006). Therefore, harnessing the impact of land surface anomalies for seasonal predictions, especially over the N.H. summer season when the SST signal is weaker than in winter, is a promising challenge that requires not only a large number of members in the ensemble set of seasonal predictions (*e.g.*, Tribbia and Baumhefner, 1998; Brankovic *et al.*, 1994), but also special care in the treatment of land surface initial conditions (*e.g.*, initial soil moisture). The treatment becomes increasingly important at higher latitudes, such as the Contiguous U.S. (CONUS) where the soil moisture feedback was found to account for more variance of monthly precipitation anomalies (Zhang *et al.*, 2008). The study by Koster *et al.* (2004) also suggested that a proper global initialization of soil moisture may enhance precipitation prediction skill during the Northern Hemisphere summer season.

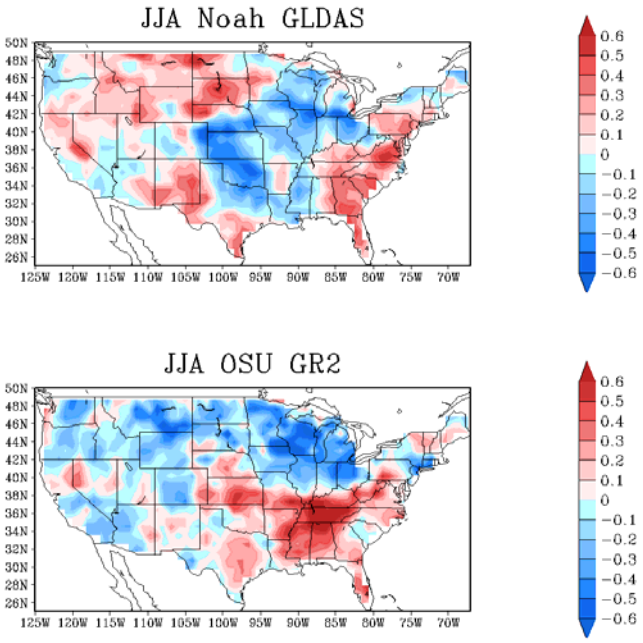

Fig. 3 Predicted JJA precipitation anomaly correlation over CONUS averaged over the 15 neutral years.

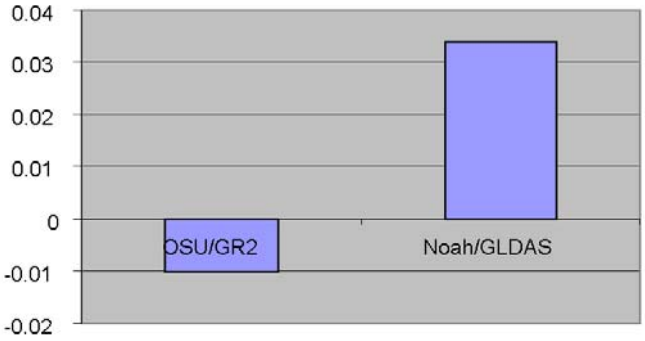

Fig. 4 CONUS-averaged predicted JJA precipitation anomaly correlation scores averaged over the 15 neutral years.

2. CFS Experiments

The next generation of NCEP Climate Forecast System (CFS) will include many advances in atmosphere, land, and ocean physics, among which the old land component (OSU/GR2 combination) used in the currently operational CFS, will be replaced with a new land component (Noah/GLDAS combination), wherein the upgrade from the OSU LSM to the Noah LSM is for inclusion of recent advances in land physics and the replacement of the old GR2 land states with the GLDAS land states is to take special care of land initializations. This study, from the land perspective, used a highly controlled approach (same atmospheric and oceanic physics, same atmospheric and oceanic initial states, same resolution, and same initial integration dates) to examine the extent to which the land upgrades (OSU to Noah LSM and GR2 to GLDAS land data assimilation system) can improve CFS summer season predictions. Experiments were first carried out over a 25-year period (1980-2004) with 10 ensemble members whose initial conditions are from mid-April to early May in fully coupled (CMIP) mode, where the old OSU LSM was initialized using the GR2 land states (CMIP OSU/GR2) and the new Noah LSM was initialized with the GLDAS land states (CMIP Noah/GLDAS). Secondly, to separate out the ocean impact, parallel experiments with both land components were also executed over the same period in an AMIP mode (*i.e.*, AMIP Noah/GLDAS and AMIP OSU/GR2), where the coupled SST was replaced by observed SST. These experiments consist of four CFS configurations. There are CMIP Noah/GLDAS, CMIP OSU/GR2, AMIP Noah/GLDAS, and AMIP OSU/GR2 respectively. Comparisons were assessed on an ensemble basis and at seasonal timescales (June-July-August: JJA). The main variable we examined is precipitation with focus over the CONUS. The main measure of CFS skill is the Anomaly Correlation (AC;

skill map), which is defined as correlation between the CFS predicted anomaly (with respect to its corresponding climatology) and the corresponding observed anomaly, where we can examine geographical patterns of the AC score, and the Area-averaged Anomaly Correlation (AAC; the bar chart), which is a single value derived from averaging the AC scores over the CONUS, where we can assess the CFS overall performance.

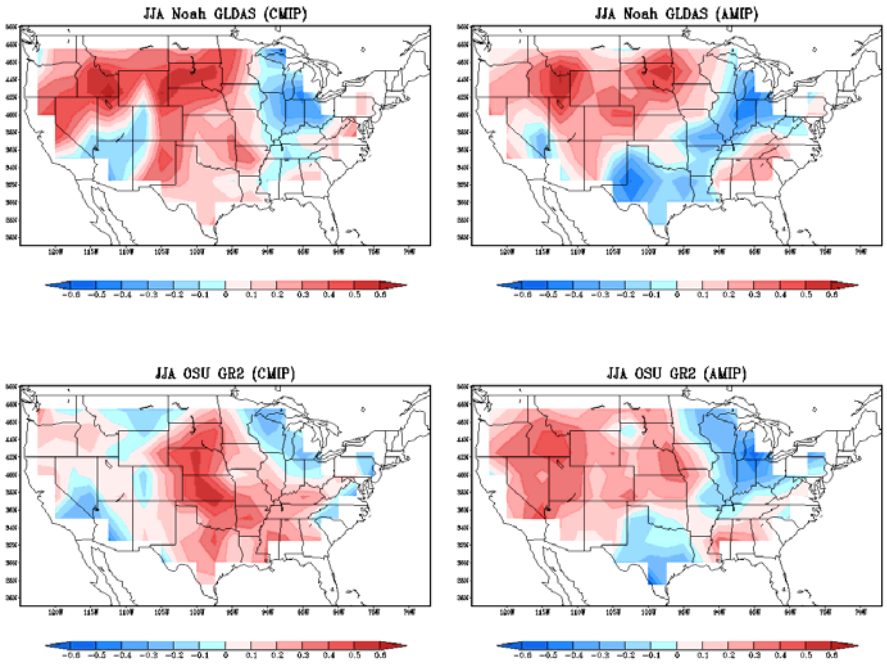

Fig. 5 JJA precipitation anomaly correlation over CONUS with CMIP (left column) and AMIP (right column) prediction modes (The left column is the same as in Figure 1, but at 2.5x2.5 degree resolution).

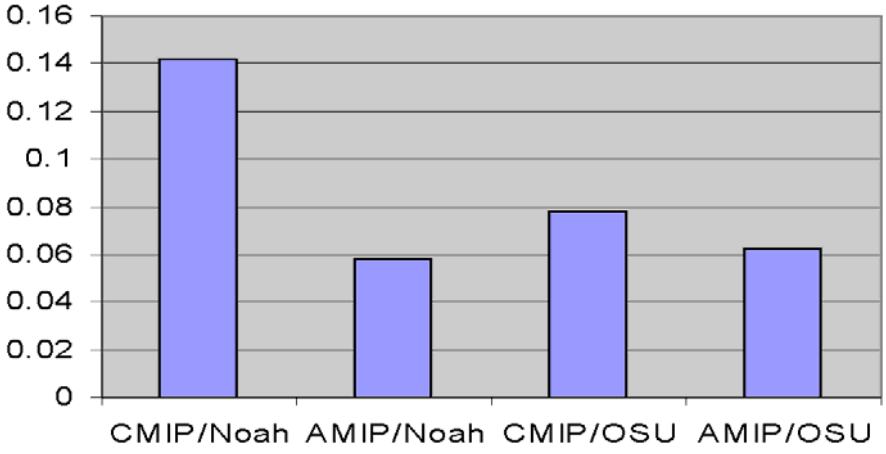

Fig. 6 CONUS-averaged JJA precipitation anomaly correlation scores with CMIP and AMIP prediction modes.

In addition to the evaluation of CFS skill over the entire 25 years, to provide insight into the difference in CFS performance with different SST signals, the 25 years are stratified into ENSO non-neutral and neutral years 3using the observed May-June-July (MJJ) Niño 3.4 SST anomaly magnitude of 0.7 ˚C as a threshold for non-neutral years (slightly lager than the commonly used 0.5˚C threshold, to better separate out ocean impact). As a result, the 25 years are split into 10 non-neutral and 15 neutral years. The non-neutral years are 1982, 1983, 1987, 1988, 1991, 1992, 1993, 1997, 1999, and 2002 (among which, only 1988 and 1999 are cold ENSO years and the rest are warm ENSO years) and the neutral years are 1980, 1981, 1984, 1985, 1986, 1989, 1990, 1994, 1995, 1996, 1998, 2000, 2001, 2003 and 2004, respectively. The CFS prediction skill with and without the land upgrades in both CMIP and AMIP modes is also assessed for the ENSO-neutral years to examine how much land-atmospheric interactions contribute to seasonal predictability.

3. Main Results

Figure1 presents the CONUS AC skill map of JJA ensemble mean total precipitation over the 25-yr reforecasts from the two CMIP CFS configurations. Checking on the CFS performance over different geographical regions, Figure 1 shows that compared to the OSU/GR2 CFS, the Noah/GLDAS CFS has a larger area of high anomaly correlation scores over a majority of the western CONUS and each configuration yields different preferred regions toward better performance where the Noah/GLDAS CFS shows a tendency

toward high scores in a majority of the Pacific Northwest and the northern Great Plains, whereas the OSU/GR2 CFS appears to yield somewhat better AC scores in the southwest monsoon region and the states that border the Gulf of Mexico. Using a different measure, the bar chart of AAC in Figure 2 clearly shows that the CFS with the new component of GLDAS/Noah yields a higher value, indicating that upgrading of the OSU/GR2 combination to the Noah/GLDAS combination does improve the overall CONUS precipitation prediction. Despite this improvement with the land component upgrade over the entire 25 years, the student's t-test indicates that the difference is not statistically significant at 90% confidence level. Looking into the CFS performance over the 15 neutral years when the land-anomaly forcing has more controls over seasonal precipitation prediction, Figures 3 and 4 are as in Figures 1 and 2 but for the 15 neutral years. Figure 3 shows that the CFS precipitation prediction skill drops dramatically with both land components when the ENSO signals are weak and the degradations mainly occur over most of the relatively drier Midwest region and the Pacific Northwest states However, the Noah/GLADS CFS maintains relatively good performance over the above regions (albeit with degradation too). As shown in Figure 4, the CONUS-averaged AC scores with both configurations are much lower than their 25-year averages, where the Noah/GLDAS CFS shows a small positive value and the OSU/GR2 CFS yields a negative number. While the values are low, the student's t-test indicates that difference is significant at 90% confidence level (the Noah/GLDAS CFS is significantly better in CMIP mode during the 15 ENSO-neutral years).

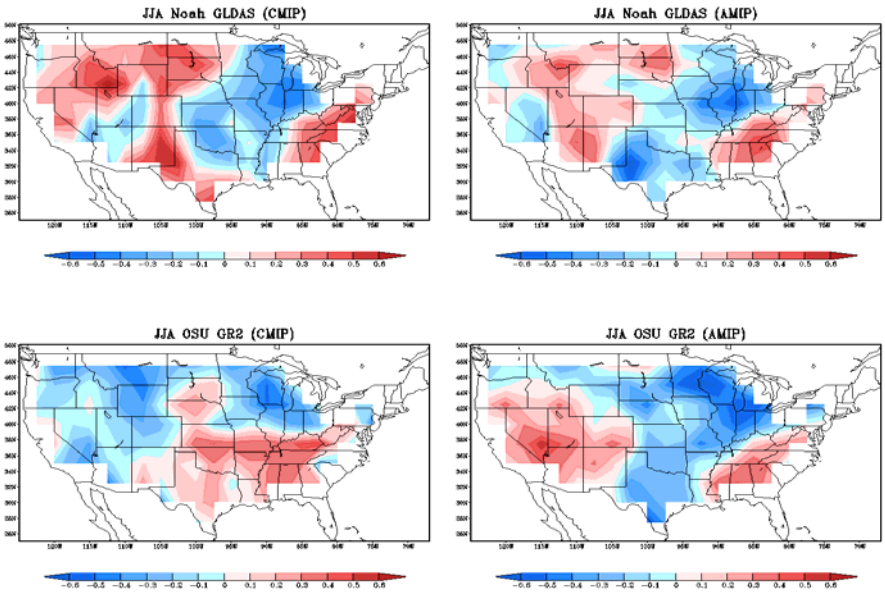

Fig. 7 JJA precipitation anomaly correlation averaged over the 15 neutral years with CMIP (left column) and AMIP (right column) modes (The left column is the same as in Figure 3, but at 2.5x2.5 degree resolution).

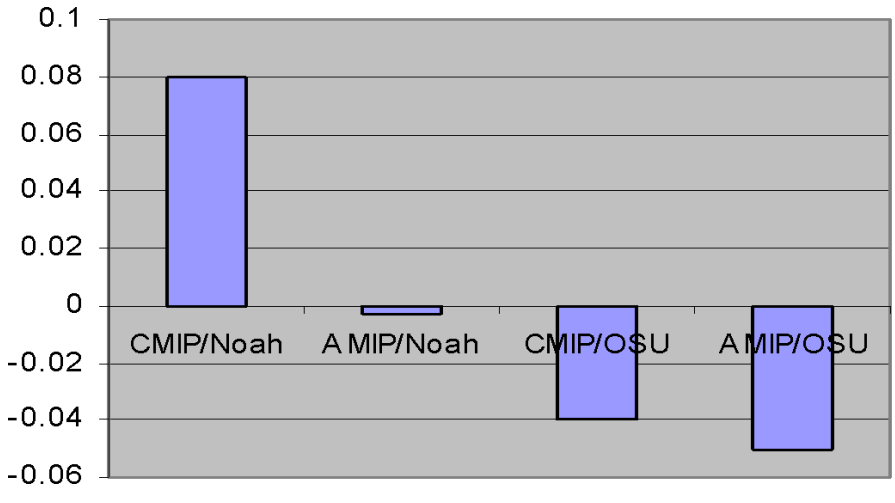

Fig. 8 CONUS-averaged JJA precipitation anomaly correlation scores averaged over the 15 neutral years with CMIP and AMIP prediction modes.

To confirm the improvement over precipitation skill is really benefited from the land upgrades and to separate out the ocean effect, an AMIP-style run was performed with both CFS configurations, where the coupled SST is replaced by the observed SST for the same 25 years. Checking on how well the CFS performs in the AMIP mode, Figure 5 presents the CONUS AC skill maps and comparison with their corresponding

coupled runs (the left column is the same as in Figure 1, but evaluated at 2.5x2.5 degree resolution to accommodate later cross-correlation analysis where the atmospheric verification data from GR2 is used. Same applies to Figure 7 below and previous Figure 3). In Figure 5, the geographic patterns of the AC skill maps with and without the land upgrades (right column) look extremely similar in the AMIP-style runs, where both CFS configurations show negative AC scores over the Midwest regions and the southern Great Plains and positive scores from the central Great Plains all the way to the Pacific Northwest. The difference lies in the magnitudes of the positive and negative values. Overall, as shown in Figure 6, the difference between the second and the fourth bar is very small and is not statistically significant at 90% confidence level. Compared to their corresponding coupled runs, the CMIP Noah/GLDAS CFS has much better performance over the southern Great Plains than the AMIP Noah/GLDAS CFS, and the CMIP OSU/GR2 CFS, except slightly degraded performance over the Pacific Northwest and the Rocky Mountains, performs better than the AMIP OSU/GR2 CFS everywhere else. On average, as also shown in Figure 6, the first bar is higher than the second bar, so is the third bar than the fourth bar. Checking on the CFS performance in AMIP mode with and without the land upgrades during the ENSO-neutral years, Figure 7 is as in Figure 5 but for the 15 neutral years. Similar to what seen in the coupled runs, the CFS skill decreases dramatically with both configurations when SST impact is weak. Both the AMIP Noah/GLDAS and the AMIP OSU/GR2 CFS have larger areas of negative AC scores than their 25-year averages. As reflected in Figure 8, the CONUS-averaged AC scores in both AMIP Noah/GLDAS (the second bar) and the AMIP OSU/GR2 CFS (the fourth bar) are negative. The difference is that the negative value is smaller with the AMIP Noah/GLDAS CFS. However, even the difference between the two negative values is small, the t-statistical test indicates that it is significant at 90% confidence level (Noah/GLDAS is significantly better than OSU/GR2 in AMIP mode during the ENSO-neutral years).

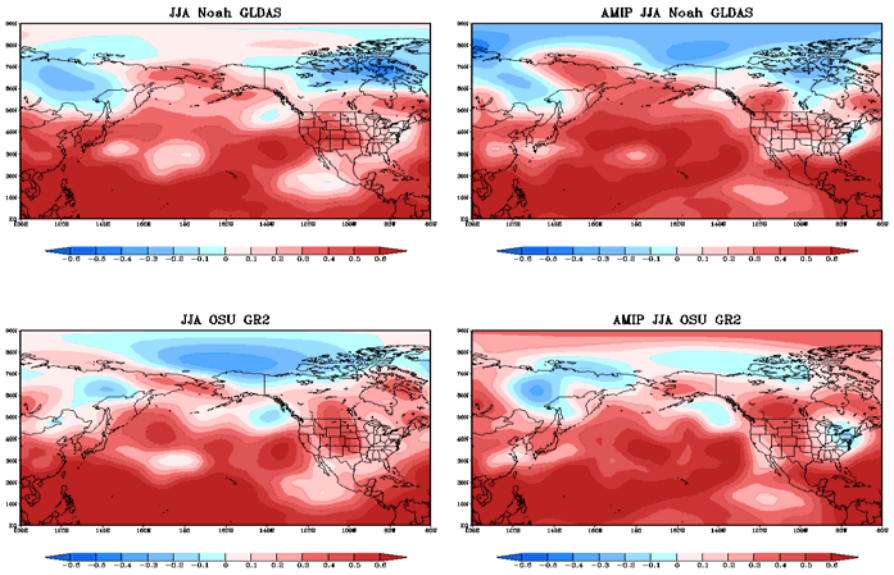

Fig. 9 JJA 500 mb GPH anomaly correlation with CMIP (left column) and AMIP (right column) prediction modes.

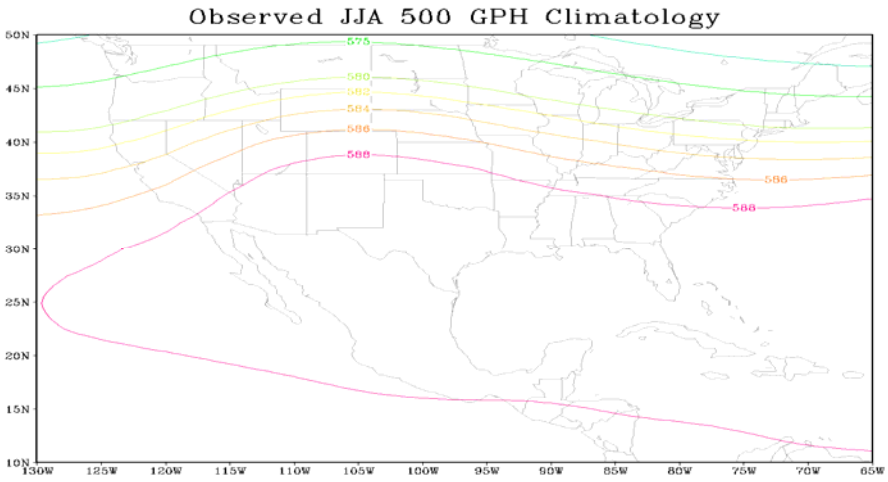

Fig. 10 JJA 500 mb GPH climatology in GR2.

To get insight into the why the AMIP-style runs are not as good as the CMIP-style runs, we examined how the land-atmosphere-ocean interactions differ with the two modes. Ocean, atmosphere and land are represented by SST, 500mb Geo-Potential Height (GPH), and soil moisture respectively. We first checked on

how SST impacts the large-scale atmospheric circulation performance in the four CFS configurations. Figure 9 presents the JJA 500mb GPH AC skill maps averaged over the 25 years. In Figure 9, the CFS in AMIP mode with both land components does a better job over most of the Pacific Ocean due to strong SST effect, but performs worse over the CONUS, especially over the Atlantic and the Gulf states than their corresponding CMIP-style runs. Looking into how well that the four CFS configurations perform in predicting JJA 500mb GPH climatology, Figure 10 presents the observed JJA 500mb GPH climatology where the extent of 588 GPH line can expand from the Four Corner states much further to the southern Mexico and the center is located over the southern Texas, which looks similar to the predicted climatology in the CMIP-style runs in Figure 11 (left column) although it's still a little bit low and the area is smaller. This is different from the climatology predicted from the AMIP-style runs (right column) where the extent of 588 GPH line is much smaller than both observation and the CMIP runs and its center is located over the state of New Mexico. This shifted center in 500mb GPH climatology causes changes in airflow patterns over the Gulf States which contribute to the skill loss as shown in Figures 5 and 7.

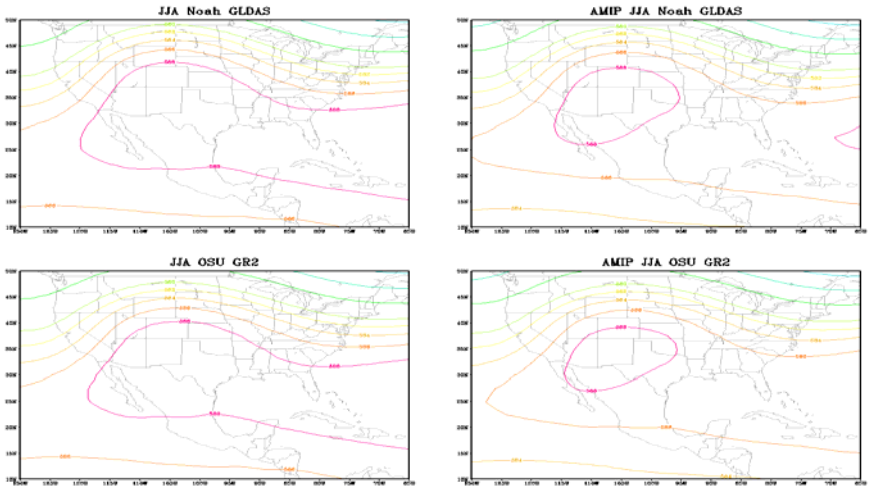

Fig. 11 Predicted JJA 500 mb GPH climatology with CMIP (left column) and AMIP (right column) modes.

Looking into how 500GPH anomaly interacts with soil moisture anomaly, Figure 12 presents their JJA anomaly cross correlations in both Noah/GLDAS and OSU/GR2 data assimilation systems. The two panels of Figure 12 show that they are all negatively correlated. The difference lies in that it is stronger in the Noah/GLDAS system. Checking on how well the CFS predicts the cross correlation in both CMIP and AMIP modes, Figure 13 shows that in the CMIP-style runs, the cross correlation with and without land upgrades has very good agreements with the observations (negatively correlated). However in the AMIP-style runs, the CFS with both land components predicts the wrong sign (positively correlated) over the Gulf and the Atlantic states. They are exactly the regions where the low JJA 500mb GPH AC skill and shifted JJA 500mb GPH climatology are located. The persistent forcing from using observed SST does not allow any feedbacks from the atmosphere and leads to changes in large-scale atmospheric circulations.

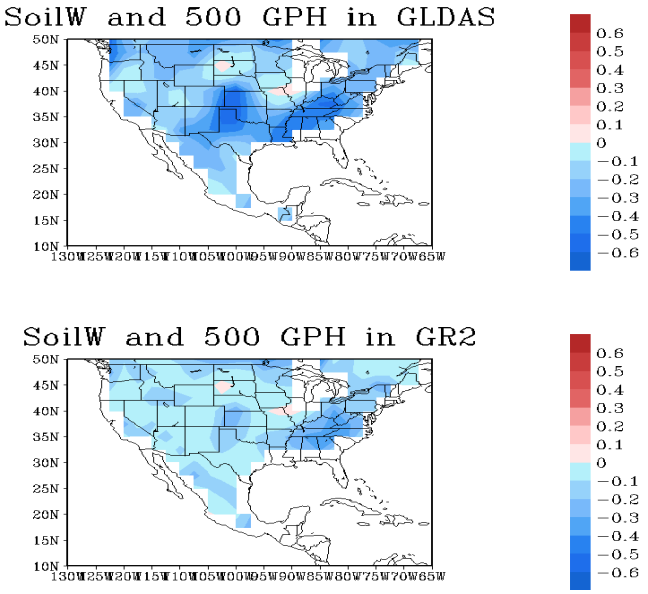

Fig. 12 JJA soil moisture and 500mb GPH anomaly cross correlation in GLDAS (top) and GR2 (bottom).

4. Conclusions

Coupled CFS experiments indicate that the land component upgrade from OSU/GR2 to Noah/GLDAS does improve the overall summer season precipitation predictions, especially during the ENSO-neutral years. Compared to the coupled runs, the CFS loses skill in the AMIP mode with both land components, but the difference is still

significant during the ENSO-neutral years, demonstrating that the improvement is really benefited from the land upgrades and more represented in the coupled mode. Ignoring any feedbacks from the atmosphere using prescribed oceanic boundary conditions will adversely affect land-atmospheric interactions, and thus degrade the CFS performance.

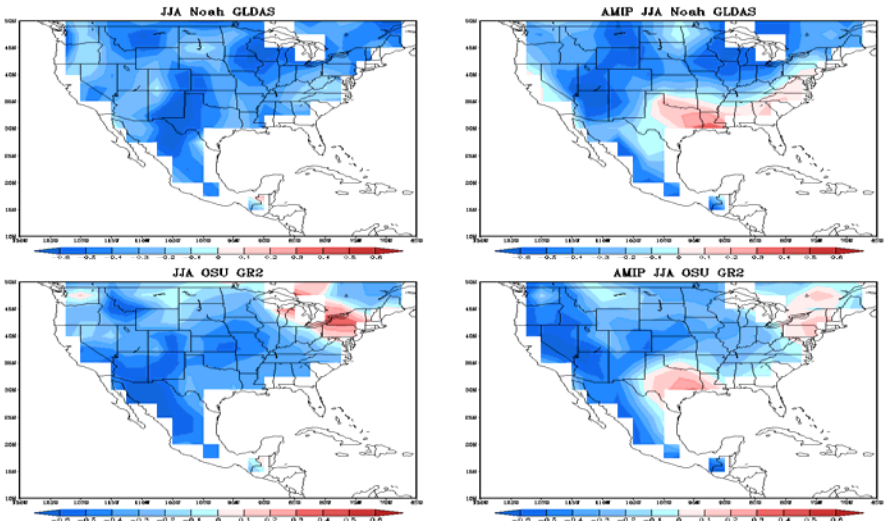

Fig. 13 Predicted JJA soil moisture and 500mb GPH anomaly cross correlation with CMIP (left column) and AMIP (right column) modes.

References

Brankovic, C., T.N. Palmer, and L. Ferranti, 1994: Predictability of seasonal atmospheric variations. *J. Climate*, **7**, 217-237.

Dirmeyer, P.A, 2001: An evaluation of the strength of land-atmosphere coupling. *J. Hydrometeorol.*, **4**, 329-344.

Lorenz, E.N., 1963: Deterministic nonperiodic flow. *J. Atmos. Sci*, **20**, 131-141.

Koster, R.D., M.J. Suarez, and M. Heiser, 2000: Variance and predictability of precipitation at seasonal-to-interannual timescales. *J. Hydrometeorol.*, **1**, 26-46.

Koster, R.D., and M.J. Suarez, 2001: Soil moisture memory in climate models. *J. Hydrometeorol.*, **2**, 558-570.

Koster, R.D., M.J. Suarez, R.W.Higgins, and H.M. Van den Dool, 2003: Observational evidence that soil moisture variations affect precipitation. *Geophys. Res. Lett.*, **30(5)**, 1241.

Koster, R.D., and Coauthors, 2004: Realistic initialization of land surface states: Impacts on subseasonal forecast skill. *J. Hydrometeorol.*, **5**, 1049-1063.

Koster, R.D., and Coauthors, 2006: GLACE: The Global Land-Atmosphere Coupling Experiment: Part 1: Overview, *J. Hydrometeorol.*, **7**, 590-610.

Shukla, J., 1998, Predictability in the midst of chaos: A scientific basis for climate forecasting. *Science*, **215**, 1498-1501.

Shukla, J., and Y. Mintz, 1982: Influence of land-surface evapotranspiration on the Earth's climate. *Science*, **282**, 728-71.

Tribbia, J. J., and D.P. Baumhefner, 1998: Estimates of the predictability of low-Frequency variability with a spectral general circulation model, *J. Atmos. Sci.*, **45**, 2306-2317.

Vinnikov, K.Y., A. Robock, N. A. Speranskaya, and C.A. Schlosser, 1996: Scales of temporal and spatial variability of midlatitude soil moisture. *J. Geophys. Res.*, **101**, 7163-7174.

Wallace, J. M., and Coauthors, 1998: On the structure and evolution of ENSO-related climate variability in the tropical Pacific: Lessons from TOGA. *J. Geophys. Res.*, **103**, 14241–14259.

Wu, W., and R.E. Dickinson, 2004: Time scales of layered soil moisture memory in the context of land-atmosphere interactions. *J. Climate*, **17**, 2752-2764.

Zhang, J., W. Wang, and J. Wei, 2008: Assessing land-atmosphere coupling using soil moisture from the Global Land Data Assimilation System and observational precipitation. *J. Geophys. Res.*, **113**, D17119, doi:10.1029/2008JD009807.

US National Oceanic and Atmospheric Administration
Climate Test Bed Joint Seminar Series
NCEP, Camp Springs, Maryland, 31 March 2010

Predictability of Monsoons in CFS

V. Krishnamurthy
Center for Ocean-Land-Atmosphere Studies, Calverton, Maryland
Department of Atmospheric, Ocean and Earth Sciences, George Mason University, Fairfax, VA

1. Introduction

It has been recognized that ocean-atmosphere interactions in the monsoon region is important and that coupled general circulation models (GCMs) are more appropriate for better simulation of the monsoon rainfall. For operational seasonal forecasts, the National Centers for Environmental Prediction (NCEP) of the United States has been using the Climate Forecast System (CFS), a fully coupled model, since 2004 (Saha *et al.* 2006). The forecast skill and the predictability of the CFS at daily and intraseasonal time scales for the South Asian and South American monsoon regions are assessed in this study. The dependence of the predictability of the South Asian monsoon on different phases of the active or break cycle of the monsoon is investigated. In the case of the South American monsoon, the daily rainfall variability is decomposed into modes of different timescales using a data adaptive method. Whether there is enhanced predictability in any of these modes of the South American monsoon is examined.

This study is based on the nine-month long retrospective forecasts generated by NCEP using the CFS. Daily forecasts starting from a 15-member ensemble of initial conditions each month are available for the period 1981-2005. These ensemble members are integrated from 15 different atmospheric initial states between 9th of the month and 3rd of the following month and three pentad ocean initial conditions centered at 11th, 21st of the month and the first day of the following month. The initial states of the ensemble starting in the period 9 April – 3 May will be referred to as May initial conditions and forecasts of this ensemble as May forecasts. Similar naming convection is used for other months. For verification, the daily NCEP-Department of Energy Reanalysis-2 (R2) data and the daily high resolution gridded rainfall data from the India Meteorological department (IMD) have been used.

A major part of the analysis to assess the predictability of the CFS and to estimate the error growth rate follows the method used by Lorenz (1982). Forecast error is the difference between the forecast and observation while the predictability error is the difference between two forecasts made by the same model. The forecast error includes the error due to the uncertainty in the initial state as well as the error due to the model imperfection. A one-day forecast can be considered as a small perturbation over the observation (or analysis) for the given day. The predictability error can then be computed as the difference between two forecasts initiated one day apart. Similarly, the differences between forecasts initiated two days apart, and so on, will provide the growth of initial errors of different magnitude. The growth rate of small errors is determined by using Lorenz's empirical formula for nonlinear error growth (Lorenz 1982).

2. Predictability of South Asian monsoon

The June-September (JJAS) seasonal climatology of precipitation over the South Asian monsoon region is fairly well simulated but with overestimation over the west coast of India and the Bay of Bengal. The 850 hPa horizontal wind is better simulated both in direction and magnitude. The seasonal cycle of the daily climatological means of four monsoon indices in the forecasts capture the observed onset, peak and withdrawal phases quite well. The ensemble spread of the rainfall indices is about 2-3 mm day^{-1}. The standard deviation of the daily rainfall anomalies in the forecasts is slightly higher over India and equatorial Indian Ocean while that of the low-level horizontal wind anomalies is generally very low compared to analyses.

The forecast errors and predictability errors were examined for rainfall over three monsoon regions. These are the Indian monsoon rainfall (IMR) over the land region of India, the extended Indian monsoon

Correspondence to: V. Krishnamurthy, Center for Ocean-Land-Atmosphere Studies, 4041 Powder Mill Road, Suite 302, Calverton, MD 20705; E-mail: krishna@cola.iges.org

rainfall (EIMR) over (70°E-110°E, 10°N-30°N) and the Asian-Australian monsoon rainfall (AAMR) over (40°E-160°E, 40°S-40°N). The pattern correlation between the daily anomalies of forecast and the daily anomalies of observation/analysis drops to a value of 0.4-0.5 in first day and takes about 12 days to reach zero in the case of individual forecasts. The temporal correlation between forecast and observation/analysis of the rainfall indices for JJAS season shows considerable interannual variability and considerable ensemble spread. The correlation is even negative in several years, which indicates that the intraseasonal variability of the forecast is out of phase with the observation/ analysis.

The growth of forecast errors was examined by computing the root mean square (RMS) of the difference in daily anomalies of rainfall indices between forecast and analysis/observation. The RMS forecast errors (averaged over all ensemble members and all years) in IMR and EIMR indices are shown in Fig. 1 for forecasts starting with May, June and July initial conditions. The errors of IMR index in May and June forecasts grow slowly until 1 June and then grow faster before reaching saturation around 1 July. The initial slow growth is related to the low standard deviation during that period. The July forecast error of the IMR index shows only faster growth. The forecast error in the EIMR index grows at the same rate in the forecasts of all three months with the difference that the initial size varies. The initial size and the growth rate in the errors of AAMR index (not shown) are same for all three months, and the errors take about 15-20 days to reach saturation. The RMS forecast errors of the IMR index initiated during active (above-normal) and break (below-normal) phases were found to grow at a faster rate and reach saturation in about 20-30 days while those starting from normal phases grow at a slower rate and reach saturation in about 50-60 days. No such distinction was found in the case of EIMR index.

Following the method of Lorenz (1982), the predictability errors were computed by considering the difference between two forecasts starting one day to four days apart. The RMS predictability errors of 1-day, 2-day, 3-day and 4-day errors in the May forecasts for IMR and EIMR indices are shown in Fig. 2. The initial size of the

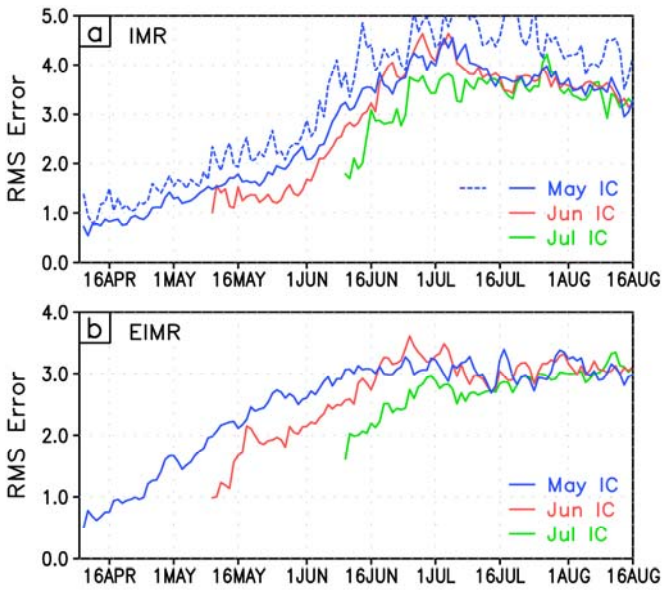

Fig. 1 Forecast errors (Forecast minus analysis) of (a) IMR index and (b) EIMR index plotted as RMS errors (averages over all available ensemble members and all years). Errors of forecasts made from May (blue), June (red) and July (green) initial conditions are shown. In (a), errors with respect to observed IMD rainfall are also shown (dashed blue). Units are in mm day^{-1}.

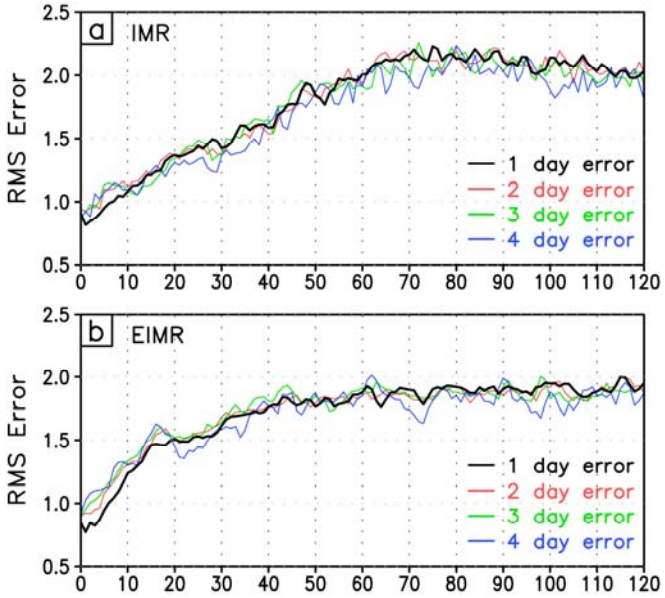

Fig. 2 RMS predictability errors of (a) IMR and (b) EIMR indices. The predictability errors are differences between two forecasts whose initial conditions differ by one day (black), two days (red), three days (green) and four days (blue). The RMS errors are average over all such errors of May initial conditions in 1981-2005.

IMR index error and the subsequent evolution are almost the same for all the four cases. The initial error is about 0.9 mm day^{-1} and takes about 70 days to reach saturation. In the case of EIMR errors, the initial size of the 1-day error is slightly less than that of the others. The EIMR errors grow slightly faster compared to the IMR errors and reach saturation in about 50 days. In the case of July forecasts (not shown), the initial size of the predictability errors is larger and the errors reach saturation in about 25 days. Quantitative estimates of the growth rates of initially small errors were obtained by using the empirical formula suggested by Lorenz (1982). The doubling time of small errors in the IMR, EIMR and AAMR indices were estimated to be 14, 9 and 5 days, respectively, for the May forecasts while the values for July forecasts were 4, 7 and 5 days, respectively. The doubling time of small errors in the IMR index for forecasts starting from active and break phases is about 2 days while the doubling time for forecasts initiated during the normal phase is 9 days.

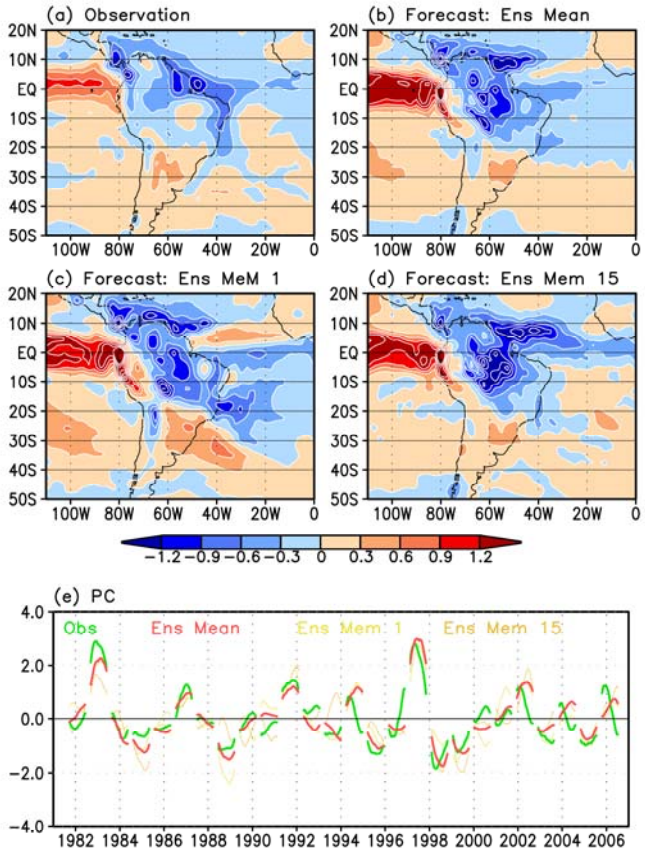

Fig. 3 Spatial structure of the rainfall ENSO mode obtained from MSSA for (a) analysis, (b) ensemble mean, (c) ensemble member 1 and (d) ensemble member 15. The corresponding daily time variability of this mode is shown in (e).

3. Predictability of South American monsoon

The December-March (DJFM) seasonal climatology of the precipitation over the South American monsoon region is fairly well simulated by the October forecast of CFS but with less rainfall over the Amazon River Basin (ARB) and more rainfall over the central-east South America (CESA) region compared to observation. The daily rainfall climatology was examined by computing the annual cycles of ARB index (average over 70°W–50°W, 5°S–5°N) and CESA index (average over 60°W–40°W, 20°S–10°S). The annual cycle of the CESA index was found to be better simulated than that of the ARB index. From the RMS forecast errors, the doubling time of small errors was found to be 6 and 9 days for the ARB and CESA indices, respectively, using the Lorenz formula. Same estimates of the doubling time of errors were obtained for the RMS predictability errors also. Both the forecast errors and the predictability errors took about 50-60 days to reach saturation.

As a new approach, the predictability of the CFS in the South American monsoon region was investigated by decomposing the forecast fields into different modes in a data adaptive manner in order to find out if there is enhanced predictability in certain modes. For this purpose, multi-channel singular spectrum analysis (MSSA) was applied on daily precipitation anomalies of forecasts and analysis. The dominant MSSA modes that were obtained consisted of a seasonally persistent mode and an oscillatory mode. The persistent mode was found to be related to the El Niño-Southern Oscillation (ENSO) variability while the oscillatory mode was found to have a period of 55 days and northeastward propagation. The spatial structure of the ENSO rainfall mode was found to be fairly well simulated by the CFS compared to the analysis, as shown in Fig. 3(a-d). The daily variability and the interannual variability of the ENSO rainfall mode was also well simulated (Fig. 3e). In the case of the intraseasonal mode, the spatial structure, period and the northeastward propagation were fairly well simulated by the model. However, the phases of the oscillation were quite different from one ensemble member to the other. The RMS forecast errors and RMS predictability errors were separately computed for the ENSO mode and the intraseasonal mode. The errors in the ENSO mode were found to grow very slowly compared to the growth of the total rainfall anomalies, as shown in Fig. 4 for

the forecast errors in the ARB index. Similar behavior was also obtained with the predictability errors and also for the CESA index. In the case of the intraseasonal oscillation, the error growth was slow but with oscillatory behavior (not shown), reflecting the fact that the phases of the oscillation are not properly simulated.

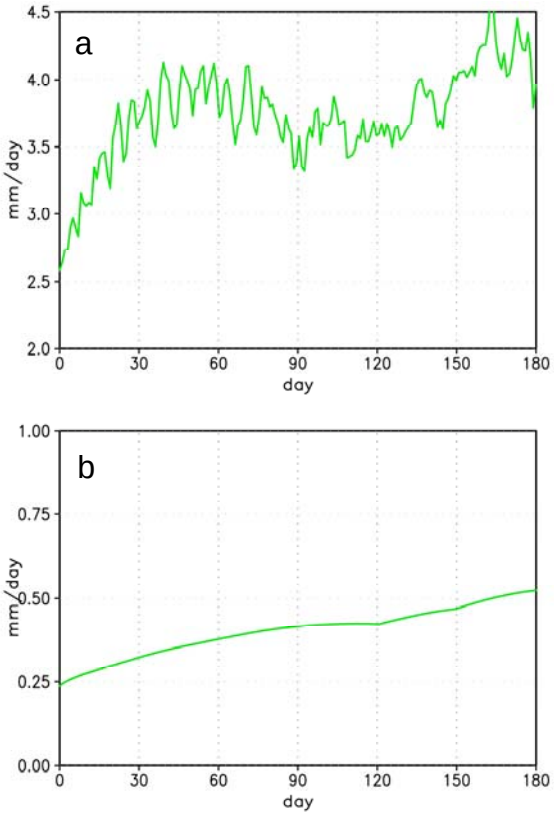

Fig. 4 RMS forecast error of ARB index in (a) total rainfall and (b) ENSO rainfall mode.

4. Conclusions

In this study, the forecast skill and predictability of the CFS have been assessed on daily and intraseasonal time scales for the South Asian monsoon region and the South American monsoon region. Using retrospective forecasts for the period 1981-2005, the growth of forecast errors and predictability errors in rainfall has been studied in detail for forecasts initiated in different months of the monsoon seasons. The growth rates of small predictability errors have been estimated by applying the Lorenz method. The doubling time of small errors for the South Asian monsoon is found to be in the range of 4-7 days for forecasts initiated in July whereas it is in the range of 5-14 days for forecasts starting in May. The growth of errors associated with forecasts which start from different phases of the monsoon intraseasonal variability has also been examined. For the rainfall averaged over the land points of India, it is found that the errors grow faster in the case of forecasts initiated during active or break phase while they grow slower with forecasts starting from normal phase. The doubling time of small errors in the South American monsoon rainfall was estimated to be in the range of 6-9 days. With a new approach, the predictability of the South American monsoon was assessed by examining the error growth of the dominant modes of the rainfall variability. It was found that the ENSO rainfall mode has very slow growth rate, providing hope for better predictability of certain features of the rainfall.

References

Krishnamurthy, V., and J. Shukla, 2008: Seasonal persistence and propagation of intraseasonal patterns over the Indian monsoon region. *Climate Dyn.,* **30**, 353–369.

Lorenz, E. N., 1982: Atmospheric predictability experiments with a large numerical model. *Tellus*, **34,** 505-513.

Saha, S., S. Nadiga, C. Thiaw, J. Wang, W. Wang, Q. Zhang, H. M. Van den Dool, H.-L. Pan, S. Moorthi, D. Behringer, D. Stokes, M. Pena, S. Lord, G. White, W. Ebisuzaki, P. Peng, and P. Xie, 2006: The NCEP Climate Forecast System. *J. Climate*, **19**, 3483-3515.

US National Oceanic and Atmospheric Administration
Climate Test Bed Joint Seminar Series
NASA, Goddard Visitor Center, Greenbelt, Maryland, 14 April 2010

Drought Monitoring and Prediction: The Recent Efforts at the Climate Prediction Center

Kingtse Mo
Climate Prediction Center, NOAA/NWS/NCEP
Camp Springs, MD, 20746

The Standardized Precipitation Index (SPI) has been used to classify the meteorological drought. The advantage is that the SPI can be derived from precipitation (P) time series alone without the need of a land-surface model. For the drought monitoring purpose, we update 3, 6, 9, 12 and 24 month SPI daily to reflect the wet and dry situations over the United States from short term (3 months) to longer term duration of 24 month.

We are developing a method to forecast 3-month SPI (SPI3) and 6-month SPI (SPI6) based on the CFS seasonal ensemble forecasts over the United States. Before predicting SPI, the P forecasts from a coarse resolution global model CFS have to be downscaled to a regional grid. In this case, we downscale from the CFS 250 km grid to a fine resolution 50 km regional grid. Four different methods of statistical downscaling and error correction are tested. The four methods are: linear interpolation, a bias correction and spatial downscaling based on the probability distribution functions (BCSD) developed by the University of Washington group, a linear regression method by John Schaake and the Bayesian method used by the Princeton University group. We tested cases with initial conditions in November, February, May and August.

The downscaled CFS P forecasts out to 6 months were appended to the precipitation analyses to form an extended P data set. The SPI was calculated from this extended time series to forecast the meteorological drought. The skill is regionally and seasonally dependent. Figure 1 shows the 6 month SPI over the U.S. is skillful out to 3 months. For the first 3 month lead time, there is no statistical significant difference among different methods of downscaling. After 3 month lead time, the Bayesian methods have small advantages because it takes into account of the hindcast skill and the spread among the CFS forecasts. However, the skill is too low to have any practical use.

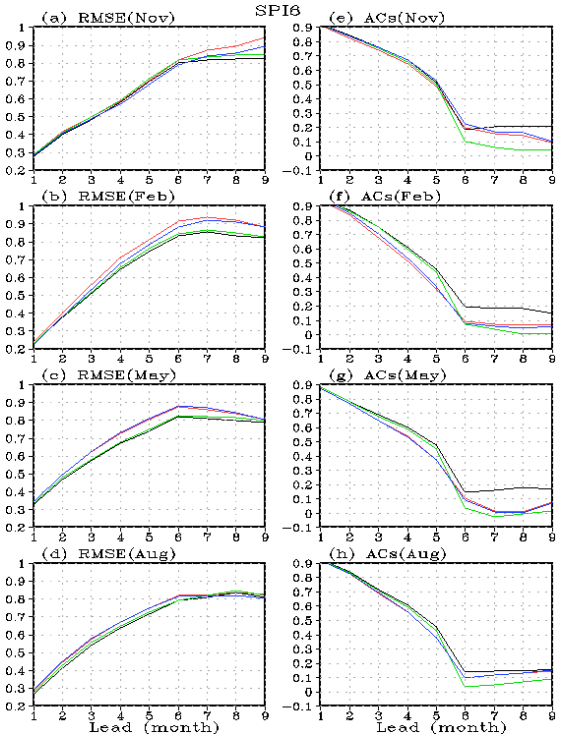

Fig. 1 Seasonal dependence of 6 month SPI forecast skill, RMSE (left) and anomaly correlation (right). From top to bottom, the initial months are November (a, e), February (b, f), May (c, g) and August (d, h). Four methods of statistical downscaling and error correction are used: linear interpolation (red), bias correction and spatial downscaling (blue), Schaake's linear regression (green), and Bayesian merging and bias correction (black).

The EMC Regional Spectral Model (RSM) group has been performing the dynamic downscaling of the CFS outputs by nesting the RSM in the CFS forecasts. The RSM has the same physics and dynamical core as the CFS and has the resolution of 50 km. While the RSM improves the P climatology, it does not improve interannual variability. For the SPI prediction, the model climatology is replaced by the observed P climatology. Therefore, there is no significant gain in skill in comparison with the Bayesian corrected T62 CFS ensemble P forecasts. To improve rainfall forecasts, the model physics is important. One can not expect to gain significant skill of P forecasts by increasing the model resolution alone.

Correspondence to: Kingtse Mo, Climate Prediction Center, NOAA/NWS/NCEP, Camp Springs, MD, 20746;
E-mail: Kingtse.Mo@noaa.gov

US National Oceanic and Atmospheric Administration
Climate Test Bed Joint Seminar Series
NASA Goddard Space Flight Center, Greenbelt, Maryland, 14 April 2010

Recent Analyses of Drought Character and Prediction

Randal Koster
Global Modeling and Assimilation Office, NASA/GSFC
Greenbelt, MD 20771

Three recent studies at the GMAO related to drought were discussed at the seminar. The first, relatively well-developed study examines streamflow prediction (quite relevant to "hydrological drought") at seasonal lead times associated with snow and soil moisture initialization. This study reveals that soil moisture initialization and snow initialization on a forecast start date contribute independently to streamflow forecast skill at seasonal leads. The paper has been submitted for publication.

A second, more preliminary study focuses on skill in the seasonal forecast of soil moisture anomalies, relevant to "agricultural drought". For this purely synthetic study, observations-based meteorological data are used to drive a 0.5ºx0.5º grid of land surface model elements covering CONUS, resulting in an 84-year offline control simulation regarded as "truth". Then, an extensive series of 5-month warm season forecasts are performed, during which the land surface is driven with the (geographically varying) climatological seasonal cycles of meteorological forcing extracted from the control simulation. Skill levels (r^2, the square of correlation of forecast vs. synthetic truth) are shown in Figure 1 for soil moisture one month into the forecast and five months into the forecast. Soil moisture memory by itself provides substantial skill at one month and even some skill at five months – soil moisture can be predicted even without information on meteorological anomalies during the forecast period. Of course, soil moisture memory is a highly model-dependent quantity. The results here are therefore not provided as a representation of nature but as a demonstration of the type of analysis that should be performed with any modeling system to isolate the contributions of model-dependent soil moisture

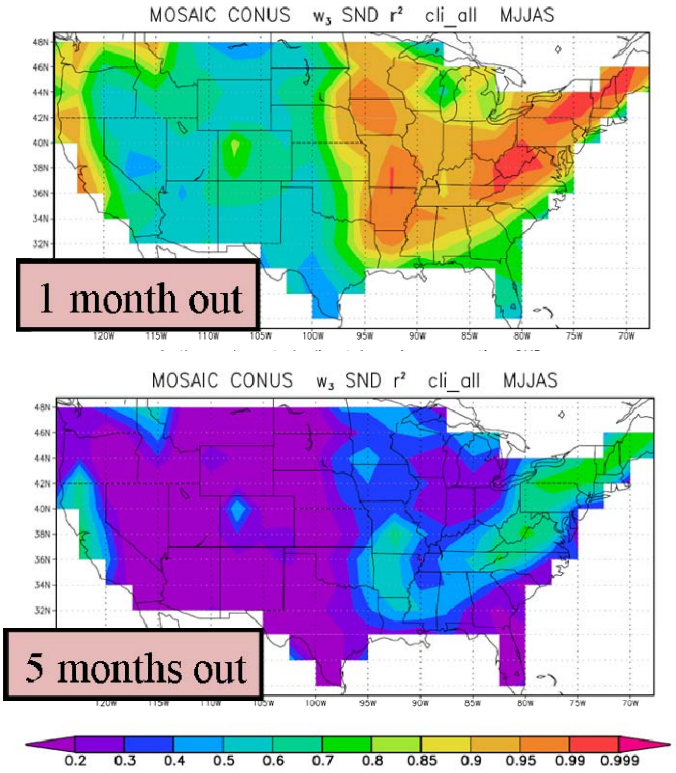

Fig. 1 Skill levels (r^2) of forecasted soil moisture versus synthetic truth, for warm season forecast starts.

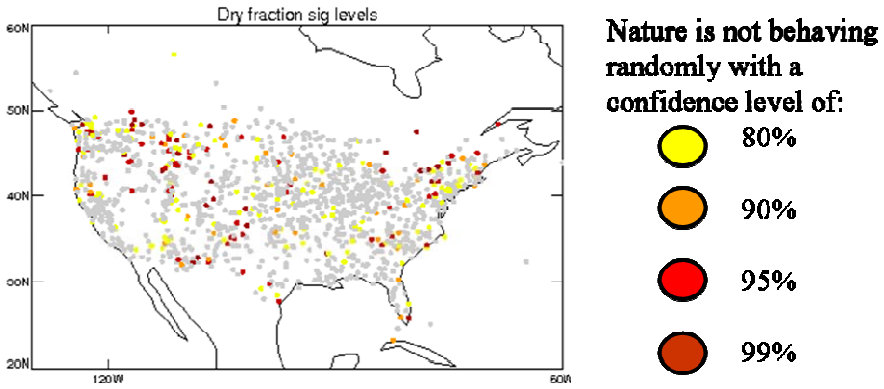

Fig. 2 Indication of the degree to which the observed occurrences of multi-year drought may be attributable to some external mechanism (see text).

Correspondence to: Randal Koster, Global Modeling and Assimilation Office, NASA/GSFC, Greenbelt, MD 20771;
E-mail: randal.d.koster@nasa.gov

memory and forecasted meteorology to forecasted soil moisture – key to understanding any soil moisture forecast. Additional analysis shows that of all the forecasted meteorological fields, precipitation is by far the most important; the others (air temperature, radiation, *etc.*) can be replaced with climatology with little impact on forecasted soil moisture.

The third (also preliminary) study examines the "attributability" of multi-year meteorological drought. Figure 2 shows a sample result. At each dot in the figure, the observational time series of annual rainfall was ranked, and a given year's rainfall was determined to be in the lower, middle, or upper tercile of all realized values. The number of times that a dry year (in the lowest tercile) followed another dry year was established, and the occurrences of such a "multi-year drought" were compared to occurrences obtained for thousands of random shufflings of the yearly historical data. At the orange dots, the actual occurrences of multi-year drought exceeded those obtained in 90% of the shufflings, indicating that the null hypothesis of "no multi-year attribution" can be rejected at the 90% confidence level. However, even with no attribution, 10% of the dots in the figure should show up orange (or darker), and in fact, roughly 10% do. The upshot of this (perhaps overly simple) analysis is that while it's natural to want to attribute multi-year drought to a physical mechanism that acts on multi-year time scales, the observational record is not inconsistent with the idea that multi-year drought is a consequence of the random clumping of independent dry years. Perhaps an external multi-year mechanism exists, but the "random juxtaposition of dry years" argument is not disproven by the data.

US National Oceanic and Atmospheric Administration
Climate Test Bed Joint Seminar Series
NASA, Goddard Visitor Center, Greenbelt, Maryland, 14 April 2010

NCEP/EMC NLDAS Support for Drought Monitoring and Seasonal Prediction

Michael Ek, Youlong Xia, and the NLDAS team
Environmental Modeling Center, NOAA/NWS/NCEP
Camp Springs, MD 20746

The North American Land Data Assimilation System (NLDAS)-phase 2 is an extension of the multi-institution NLDAS-phase 1 pilot project (Mitchell et al 2004), and is a cooperative project with NASA/Goddard/HSB, Princeton University, University of Washington, NOAA/NWS Office of Hydrologic Development (OHD), and other researchers and NOAA CPO/CPPA partners.

NLDAS consists of four land models executed in an uncoupled mode using atmospheric forcing to yield surface fluxes and evolving land states. The land models are run at 1/8th-degree resolution over the continental US, and include Noah (from NCEP), VIC (Princeton), Mosaic (NASA), and SAC (NWS OHD). The atmospheric forcing data comes from the real-time extension of the North American Regional Reanalysis based on the mesoscale NAM/Eta model from c. 2003 (Mesinger et al 2006), with GOES-based bias-corrected incoming solar radiation, and observed daily gauge precipitation disaggregated to hourly using radar-based estimates. NLDAS has been run from 1979 to present in a retrospective mode, including a 15-year spin-up, with a 30-year climatology available for each model; output includes surface fluxes and hydrological land-state variables such as soil moisture, snowpack, and runoff. Figure 1 shows variation of the correlation between observed and simulated monthly soil moisture anomaly with month and soil depth. Soil moisture is averaged over the 17 sites of Illinois State to calculate its anomaly and correlation. All models show high simulation skills for all seasons except for winter, particularly for late spring and early fall although Mosaic model has lower skills than the other models. Low simulation skills for four models are closely associated with inability of models in simulating frozen soil and snowmelt processes. High simulation skills are because there is strong relationship between monthly mean precipitation and soil moisture anomaly.

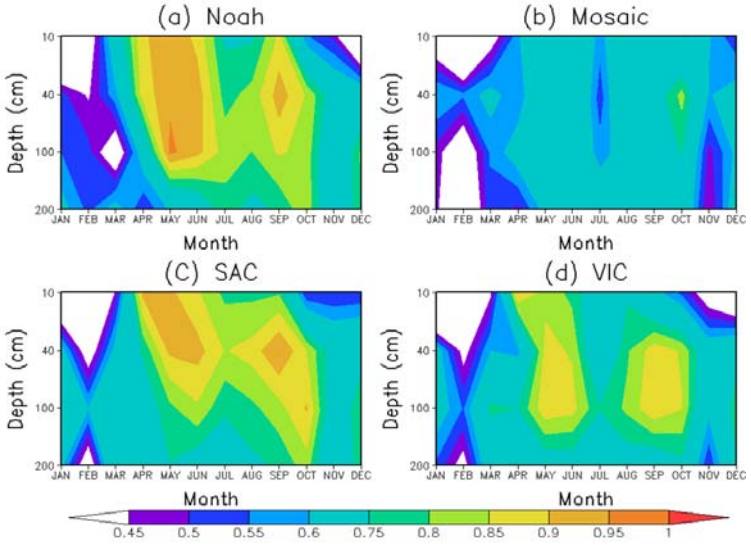

Fig. 1 Seasonal variation of the correlation between observed and simulated monthly soil moisture anomaly averaged over 17 Illinois sites using the four land surface models including (a) Noah, (b) Mosaic, (c) SAC, and (d) VIC for the period during 1985 and 2004 and four soil layers.

A companion uncoupled seasonal hydrological prediction system uses the VIC land model driven by seasonal forecasts from three sources for the required surface forcing: Ensemble Streamflow Prediction (ESP), NCEP Climate Prediction Center (CPC) Official Seasonal Outlook, and NCEP CFS ensemble dynamical model prediction. Twenty ensemble members (via a Bayesian-merging algorithm) are used to generate 1-6 month ensemble seasonal prediction products, e.g. soil moisture, runoff, streamflow, etc. Figure 2 shows ensemble-mean baseflow (part of streamflow) anomaly forecast for January-June 2010. The first two-month forecast shows very similar spatial patterns for all three approaches. From the third month, three

Correspondence to: Michael Ek, Environmental Modeling Center, NOAA/NWS/NCEP, Camp Springs, MD20746;
E-mail: Michael.Ek@noaa.gov

predictions display obvious differences. For example, CFS shows a negative anomaly, the CPC shows a positive anomaly, and the ESP shows an in-between result. In spite of the distinct differences among three predictions, similar variation tendencies can be found. Certainly, the quality of the products needs to be further evaluated by using USGS gauge streamflow measurement.

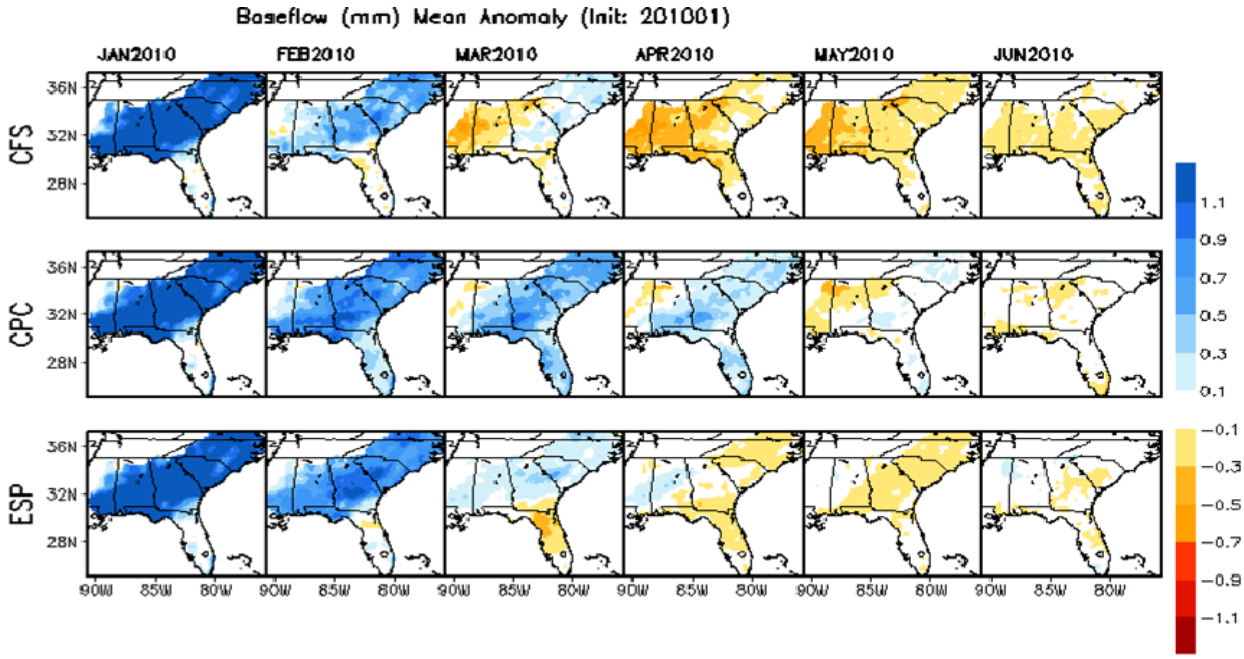

Fig. 2 Six-month forecast of ensemble-mean baseflow anomaly made by the VIC model using three surface forcing seasonal forecasts of the NCEP CFS ensemble dynamic model prediction (top), NCEP CPC Official Seasonal Outlook (middle), and Ensemble Streamflow Prediction (bottom).

The motivation for NLDAS-2 is to support drought monitoring and seasonal drought prediction at CPC, and for the National Integrated Drought Information System (NIDIS, drought.gov) by providing NLDAS multi-model analysis, monitoring, and seasonal prediction products. (See www.emc.ncep.noaa.gov/mmb/nldas.) NLDAS datasets include the forcing data, and output from the four models, staged on NCEP public servers: nomad6 for real-time runs, and ldas3 for retrospective (see: www.emc.ncep.noaa.gov/mmb/nldas/Download_Public_users.txt), and at the NASA Earth Science Data and Information Service Center (disc.sci.gsfc.nasa.gov/hydrology/data-holdings).

References

Mesinger, F. and co-authors, 2006: North American Regional Reanalysis. *Bull. Amer. Meteorol. Soc.*, **87**(3), 343–360, DOI: 10.1175/BAMS-87-3-343.

Mitchell K. E., and co-authors, 2004: The multi-institution North American Land Data Assimilation System (NLDAS): Utilizing multiple GCIP products and partners in a continental distributed hydrological modeling system. *J. Geophys. Res.*, **109**, D07S90, doi:10.1029/2003JD003823.

US National Oceanic and Atmospheric Administration
Climate Test Bed Joint Seminar Series
ESSIC/UMD, College Park, Maryland, 10 May 2010

Variability and Prediction of the Asian and Indo-Pacific Monsoon Climate in the NCEP Climate Forecast System

Song Yang

Climate Prediction Center, NOAA/NWS/NCEP
Camp Springs, MD, 20746

1. Introduction

The NCEP Climate Forecast System (CFS) is one of the state-of-the-art global models that have been applied to understand and predict the variability of global climate. It is one of the important tools for the official forecasts of U.S. monthly and seasonal temperature and precipitation at the NOAA Climate Prediction Center. CFS products are also becoming an important source of information for regional climate predictions in many countries outside the U.S.

In this presentation, a comprehensive review of the characteristics of monsoon climate over the Asian and Indo-Pacific sector in the NCEP CFS and the skill of monsoon prediction by the system is provided. Particular emphasis is placed on the impacts of El Niño-Southern Oscillation (ENSO), Indian Ocean (IO) sea surface temperature (SST), land surface process, ocean-atmosphere coupling, and model resolutions. Results from model evaluation by advanced tools are also discussed.

The presentation is based on the results from the studies of Yoo *et al.* (2006), Yang *et al.* (2008a, b), Liang *et al.* (2009), Gao *et al.* (2010), Li and Yang (2010), Yang *et al.* (2010), and Yoo *et al.* (2010). The model output analyzed includes the following products: (1) 15-member retrospective prediction runs of the CFS, an operational version in resolution T62, (2) a set of 10-member hindcasts of the CFS in T126 for different land models and land initial conditions, and (3) free runs of the model in both T62 and T126. The above studies also employ the following (re)analysis and observational data sets: the NCEP-NCAR reanalysis, CPC CMAP precipitation, NOAA SST, and CPC surface temperature analysis.

2. Results

(a) Summer monsoon

For the Asian summer monsoon, several major features have been revealed:

(i) Figure 1 shows the summer climatology of CMAP precipitation, CFS precipitation, and their difference. Figure 1a illustrates several centers of observed precipitation over western India, Bangladesh-Burma, Indo-China peninsula, South China Sea, and east of the Philippines, with the highest center over Bangladesh, Burma, and northern Bay of Bengal. It also shows large precipitation over the tropical central-eastern IO and the Meiyu rain band over eastern China, Baiu over Japan, and Changma over Korea. Furthermore, the figure shows relatively lighter precipitation over the eastern Indian coast, east of Indo-China peninsula, and the northwestern Pacific. Light precipitation is also seen over the western

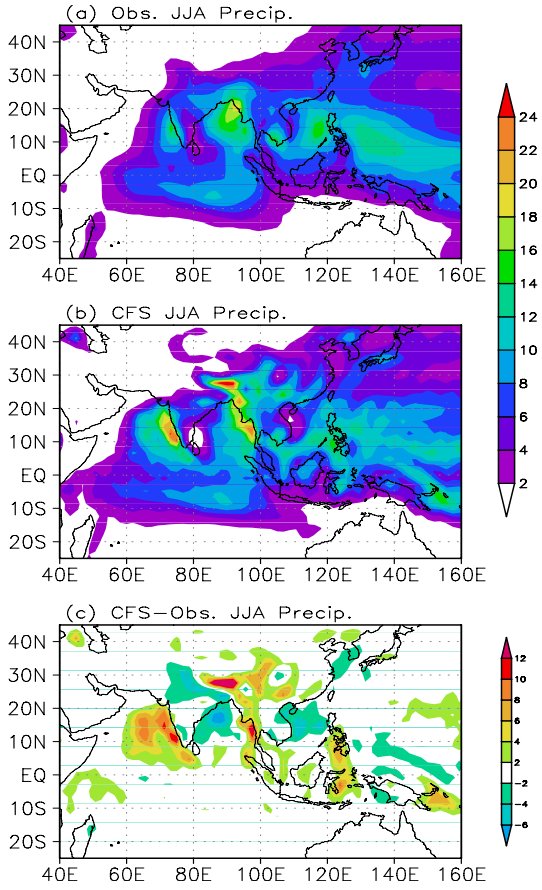

Fig. 1 Fig. 1. (a) 1981-2003 climatology of JJA precipitation from CMAP, (b) 1981-2003 climatology of JJA ensemble-mean precipitation from CFS T62 (zero month lead), and (c) difference between (b) and (a). Units: mm per day.

Correspondence to: Song Yang, Climate Prediction Center, NOAA/NWS/NCEP, Camp Springs, MD, 20746;
E-mail: Song.Yang@noaa.gov

Arabian Sea where ocean upwelling driven by monsoon flow cools the sea surface. Comparison between Figs. 1a and 1b indicates that the CFS captures the general features of observed precipitation quite well. For example, the model captures the locations of major high and low centers of monsoon precipitation. The model precipitation and observed precipitation also compare reasonably well in magnitude in many places. A merit of the CFS appears in simulating the East Asian Meiyu rain band and the precipitation over the tropical IO. In particular, while general circulation models often fail to produce the Meiyu rain band, the CFS captures the phenomenon of precipitation reasonably well, in spite of an underestimation of precipitation over Korea and the Yellow Sea. The CFS performs well in capturing the tropical IO precipitation center, for which many models even fail in reproducing the shape of the precipitation center. However, the CFS overestimates the precipitation over the eastern Arabian Sea, the Himalayas, and Burma, and underestimates the precipitation over northwestern Bay of Bengal, northern India, and South China Sea (see Fig. 1c). The overestimation of precipitation over the southern-southeastern hills of the Tibetan plateau seems one of the main problems of monsoon simulations by the model.

(ii) The skill of prediction of several dynamical monsoon indices can be seen from Fig. 2. The CFS is highly skillful in predicting the large-scale Asian summer monsoon circulation, as seen in the confidence of predicting the monsoon measured by the Webster-Yang monsoon index (Webster and Yang 1992), which exceeds the 99% confidence level (R=0.52; Student *t*-test) using the initial conditions (ICs) of January (4 months lead (LM4)) and the 95% level (R=0.41) using the ICs of December (LM5). The Southeast Asian monsoon (measured by Goswami *et al.* 1999) can be predicted at the 99% confidence level using the ICs of April and at the 95% confidence level using the ICs of March. In addition, the South Asian monsoon (measured by Wang and Fan 1999) is also predictable at the 95% confidence level using the ICs of April. However, no skill is found in predicting the East Asian monsoon (measured by Lau *et al.* 2000).

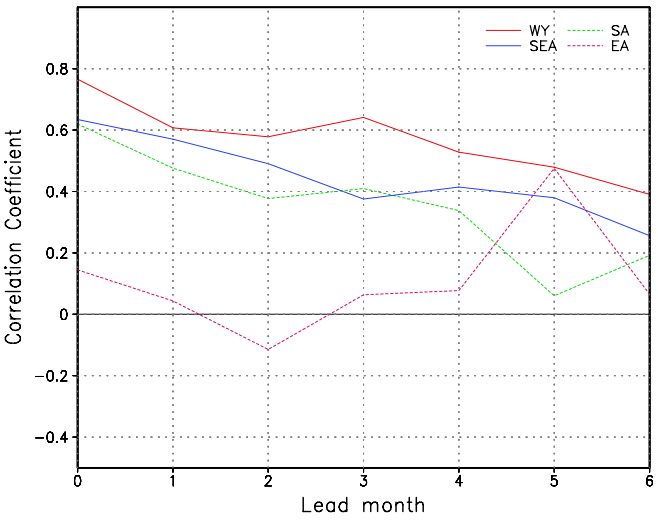

Fig. 2 The coefficients of correlation between the CFS T62 predicted and observed monsoons for different lead months. Values are shown for different dynamical monsoon indices.

(iii) It is found that the skill of monsoon prediction by the CFS comes mainly from the impact of ENSO. The most predictable patterns of monsoon rainfall depicted by the empirical orthogonal function (EOF) analysis with maximum signal-to-noise ratio (MSN) exhibit many features that are seen from the rainfall anomalies associated with the influence of ENSO. Nevertheless, the ENSO-monsoon relationship in the CFS is stronger than that observed. As observed, there are apparent relationships between the various monsoon components and IO SST especially the SST over southern IO. However, these relationships disappear or become much weaker in AMIP experiments in which the atmosphere and oceans are not coupled.

(iv) Figures 3a-c show the climatological patterns of observed summer precipitation and 850-mb winds and the difference in precipitation and winds between CFS T62 and observations. Over the Asian continent, the CFS T62 has difficulties in simulating the precipitation near the Tibetan plateau (Fig. 3b). It underestimates the precipitation over northern India and overestimates the precipitation over western China. These problems become less serious in T126 than in T62 (compared Fig. 3b and Fig. 3c). More apparent improvement in precipitation and atmospheric circulation simulations from T62 to T126 can be found for September-November (Figs. 3d-f). Figures 3e-f indicates an improvement in SON precipitation simulation over western and eastern Asia including India and China. The largest improvement occurs over the tropical Indian Ocean. For example, the CFS T62 has difficulty in simulating the climatological zonal dipole structure and its associated atmospheric circulation near the equator. In T126, the dipole structure has been simulated much more realistically, as reflected by the smaller model-observation differences in precipitation and winds.

These results suggest a better simulation of the Asian summer monsoon by the next generation of the CFS whose atmospheric component has a horizontal resolution of T126. The apparent improvement in simulating the Asian monsoon from T62 to T126 is in a sharp contrast to the simulation of the North American monsoon in which little improvement is seen from T62 to T126 for the monsoon rainfall over Southwest U.S. (Yang *et al.* 2009).

(v) In spite of the high skill of the CFS in simulating and predicting the variations (anomalies) of the large-scale patterns of the Asian monsoon, a weak bias can be clearly seen. We attribute the weak monsoon circulation in the CFS to the cold bias in the model over the much of the Asian continent, which causes a weaker-than-observed thermal contrast between the continent and oceans. As shown in Fig. 4, several experiments using CFS T126 with the current 2-level Oregon State University land model and the advanced 4-level Noah land model indicate a clear improvement. For example, the cold bias over the Asian continent is significantly reduced in the experiment using the Noah model, leading to improvements in temperature and precipitation simulations. The result suggests a better simulation of the Asian summer monsoon by the next generation of the CFS in which the Noah land model is used. (It should be pointed out that the difference between the land ICs from NCEP-DOE global reanalysis II (R2) and those from the Global Land Data Assimilation System (GLDAS) is usually small.)

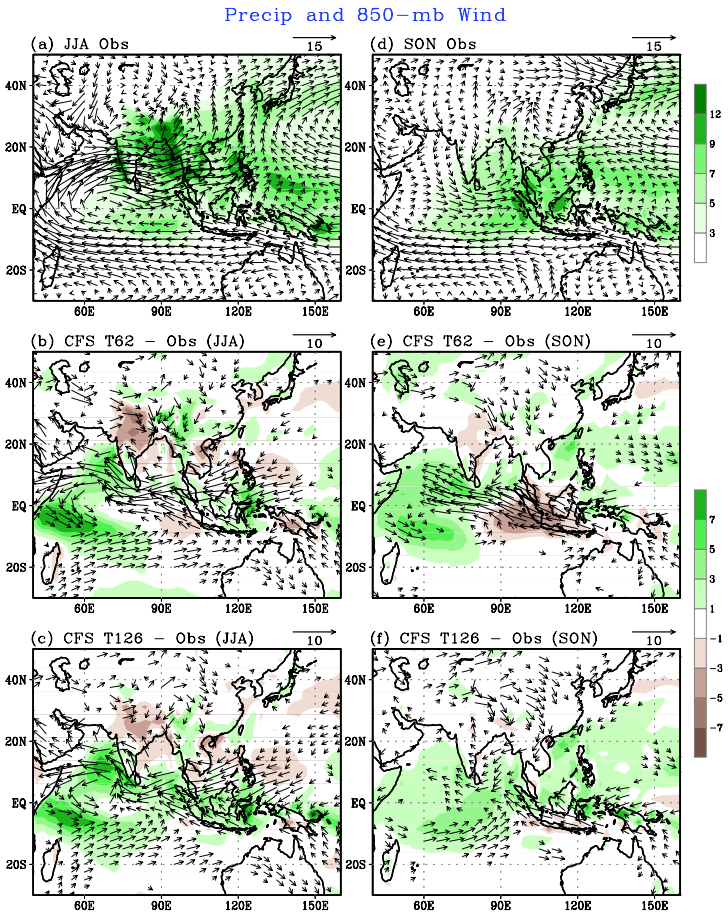

Fig. 3 1951-2005 climatological patterns of precipitation and 850-winds (NCEP-NCAR reanalysis) for JJA (a) and SON (d). (b) and (e): Differences in precipitation and winds between CFS T62 and observations. (c) and (f): Differences in precipitation and winds between CFS T126 and observations. The climatologies of 45 years are used for CFS.

(b) Winter monsoon

The East Asian winter monsoon appears prominently not only at the lower troposphere but also at the upper troposphere. It interacts with both extratropical and tropical processes. We thus define a new dynamical monsoon index so that it links to the monsoon-related atmospheric systems or parameters at both lower and upper troposphere and is able to depict the association of the monsoon with the Arctic Oscillation and ENSO. In both observations and the CFS, the index is strongly associated with the Siberian high, the East Asian trough, the East Asian and northwestern jet stream, and the lower-tropospheric meridional wind and air temperature over East Asia (Fig. 5 and figures not shown here). It is significantly related to the first EOF modes of the respective fields including sea level pressure, 500-mb height, 200-mb zonal wind, 850-mb meridional wind, and surface air temperature. The CFS can predict the newly-defined winter monsoon index in advance by 4 months, using the ICs in August, with a reasonable skill. A comparison of this index with several major previous indices used commonly indicates that the new index is most predictable, in term of the highest skill and the longest lead time.

(c) East Asian Mei-yu

Here, we focus on the Mei-yu over China, Baiu over Japan, and Changma over Korea during June-July and refer to them as East Asian Mei-yu (EAMY). Compared to the tropical monsoons, the subtropical-extratropical EAMY is relatively less predictable and the studies of the climatic characteristics of EAMY are largely infrequent.

Despite that climate models face tremendous difficulties in simulating and predicting EAMY, the NCEP CFS has demonstrated skill in capturing the Mei-yu rain bands and many large-scale features associated with EAMY. In both observations and the CFS, the EAMY is strongly associated with ENSO, subtropical northwestern Pacific high, and large-scale water vapor transport. As for tropical monsoons, air-sea interaction is important for simulating and predicting EAMY, as indicated by a comparison between the CFS hindcast and uncoupled AMIP experiments with the CFS atmospheric model. A maximum signal-to-noisy EOF analysis shows that the EAMY is the most predictable mid-summer rainfall pattern of the East Asian summer monsoon system (see Fig. 6). It is also shown that the CFS can predict the June-July EAMY in advance by one month with the ICs in May with a reasonable skill.

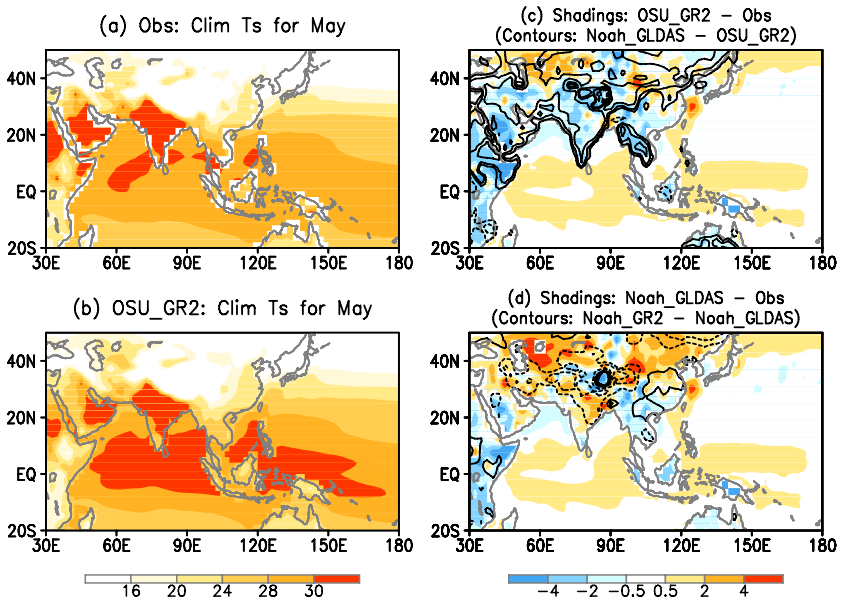

Fig. 4 Climatological patterns of May SST and surface air temperature over lands (ºC) for (a) observations, (b) OSU_GR2, and (c-d) the differences in temperature between observations and CFS output. The shadings in (c) measure the difference between observations and OSU_GR2 and those in (d) measure the difference between observations and Noah_GLDAS. The contours in (c) are for the difference between Noah_GLDAS and OSU_GR2 and those in (d) for the difference between Noah_GR2 and Noah_GLDAS (contour levels: -2, -1, -0.5, 0.5, 1, and 2).

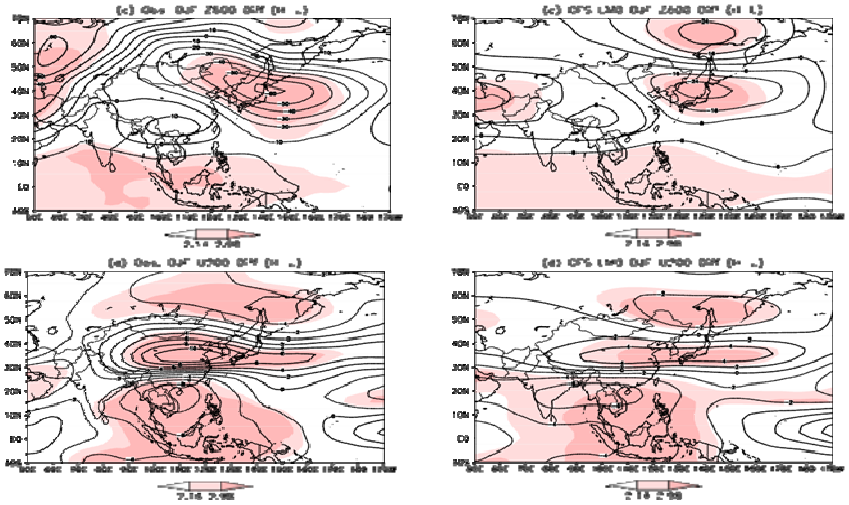

Fig. 5 Composite differences in observed 500-mb geopotential height (a) and 200-mb zonal wind (b) between high values and low values of the newly-define East Asian winter monsoon index. (c) and (d) are the as in (a) and (b), but for the NCEP CFS.

References

Gao, H., S, Yang, A. Kumar, Z.-Z. Hu, B. Huang, Y. Li, and B. Jha, 2010: Variability of the East Asian Meiyu and simulation and prediction by the NCEP Climate Forecast System. *J. Climate*, conditionally accepted.

Goswami, B. N., B. Krishnamurthy, and H. Annamalai, 1999: A broad-scale circulation index for interannual variability of the Indian summer monsoon. *Quart. J. Roy. Meteor. Soc.*, **125**, 611-633.

Lau, K.-M., K.-M. Kim, and S. Yang, 2000: Dynamical and boundary forcing characteristics of regional components of the Asian summer monsoon. *J. Climate*, **13,** 2461-2482.

Li, Y., and S. Yang, 2010: A dynamical index for the East Asian winter monsoon. *J. Climate*, in press.

Liang, J., S. Yang, Z.-Z. Hu, B. Huang, A. Kumar, and Z. Zhang, 2009: Predictable patterns of Asian and Indo-Pacific summer precipitation in the NCEP CFS. *Climate Dynamics*, **32,** 989-1001.

Wang, B., and Fan, Z., 1999: Choice of South Asian monsoon indices. *Bull. Amer. Meteor. Soc*., **80**, 629-638.

Webster, P. J., and S. Yang, 1992: Monsoon and ENSO: Selectively interactive systems. *Quart. J. Roy. Meteor. Soc.*, **118,** 877-926.

Yang, S., M. Wen, and R. W. Higgins, 2008a: Sub-seasonal features of the Asian summer monsoon in the NCEP Climate Forecast System. *ACTA Oceanologica Sinica*, **27,** 88-103.

Yang, S., Z. Zhang, V. E. Kousky, R. W. Higgins, S.-H. Yoo, J. Liang, and Y. Fan, 2008b: Simulations and seasonal prediction of the Asian summer monsoon in the NCEP Climate Forecast System. *J. Climate*, **21,** 3755-3775.

Yang, S., Y. Jiang, D. Zheng, R. W. Higgins, Q. Zhang, V. E. Kousky, and M. Wen, 2009: Variations of U.S. regional precipitation and simulations by the NCEP CFS: Focus on the Southwest. *J. Climate*, **22,** 3211-3231.

Yang, S., M. Wen, R. Yang, K. E. Mitchell, R. W. Higgins, and J. Meng, 2010: Impacts of land surface models and land surface initial conditions on the onset of Asian summer monsoon in the NCEP CFS. *J. Hydrometeor.*, to be submitted.

Yoo, S.-H., S. Yang, and C.-H. Ho, 2006: Variability of the Indian Ocean sea surface temperature and its impacts on Asian-Australian monsoon climate. *J. Geophys. Res.*, **111,** D03108, doi:10.1029/2005JD006001.

Yoo, S.-H., J. Fasullo, S. Yang, and C.-H. Ho, 2010: Relationship between Indian Ocean SST and the transition from El Niño to La Niña. *J. Geophys. Res.*, in press.

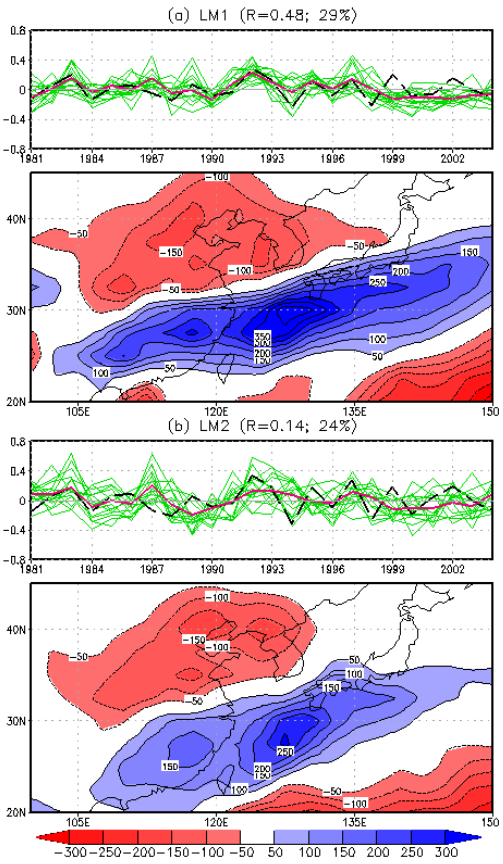

Fig. 6 First MSN EOF mode of the CFS EAMY precipitation (mm) for LM1 (a) and LM2 (b) and the corresponding time series. For the time series, thick red and thin green lines are the PCs of ensemble means and individual members, respectively. The thick black lines represent the PCs computed by projecting the observed precipitation upon the pattern of the first mode of CFS precipitation. R measures the correlation between the observation and the ensemble mean. Contour interval is 50.

US National Oceanic and Atmospheric Administration
Climate Test Bed Joint Seminar Series
NCEP, Camp Springs, Maryland, 19 October 2009

Pathogens, HABs, Swine Flu: What Can CTB Do?

Raghu Murtugudde
Earth System Science Interdisciplinary Center (ESSIC)
University of Maryland, College Park, MD

ABSTRACT

Seasonal predictions from global climate models have been used with some success for various applications for resource management and human health. Even as the resolutions of the global climate models gets finer they are expected to remain at order kilometers if not coarser for many years to decades to come. It is evident that the day-to-day management of resources and human health and planning the adaptation and mitigation strategies for future management will require information at meter scales with a keen understanding of regional specificities. A combination of dynamic and statistical downscaling is clearly the path forward and a prototype will be discussed not only for downscaling of the climate predictions but forecasting of linked Earth System parameters like pathogens, harmful algal blooms, and early attempts to drive towards respiratory disease morbidities. Computational social science is being used to project scenarios of rapid spreading of communicable diseases like swine flu and the same approach is being explored for optimizing the web of sensors to monitor the Earth System to validate, improve, and assess the skill of forecasts. How can the CTB goals be dovetailed with the needs for regional Earth System prediction and make the two way communication seamless to cover both global governance issues and regional sustainable management issues at days to decades? The discussion used a *regional Earth System prediction prototype* [(1)] to raise the relevant issues.

Paper published

[(1)] Murtugudde, R., 2009: Regional Earth System prediction: a decision-making tool for sustainability? *Current Opinion in Environmental Sustainability*. **1**, Elsevier, 37-45.

Correspondence to: Raghu Murtugudde, Earth System Science Interdisciplinary Center (ESSIC), University of Maryland, College Park, MD; E-mail: ragu@essic.umd.edu

US National Oceanic and Atmospheric Administration
Climate Test Bed Joint Seminar Series
IGES/COLA, Calverton, Maryland, 19 November 2009

The NCEP GODAS Ocean Analysis of the Tropical Pacific Mixed Layer Heat Budget on Seasonal to Interannual Time Scales

Yan Xue

Climate Prediction Center, NOAA/NWS/NCEP
Camp Springs, MD, 20746

ABSTRACT

The mixed layer heat budget in the tropical Pacific is diagnosed using pentad (5 day) averaged outputs from the Global Ocean Data Assimilation System (GODAS), which is operational at the National Centers for Environmental Prediction (NCEP). The GODAS is currently used by NCEP's Climate Prediction Center (CPC) to monitor and to understand El Niño and La Niña in near real-time. The purpose of our study is to assess the feasibility of using an operational ocean data assimilation system to understand SST variability.

The climatological mean and seasonal cycle of mixed layer heat budgets derived from GODAS agree reasonably well with previous observational and model based estimates. However, significant differences and biases were noticed. Large biases were found in GODAS zonal and meridional currents, which contributed to biases in the annual cycle of zonal and meridional advective heat fluxes. The warming due to tropical instability waves in boreal fall is severely underestimated due to use of 4-week data assimilation window. On interannual time scales, the GODAS heat budget closure is good for weak-to-moderate El Niños. A composite for weak-to-moderate El Niños suggests that zonal and meridional temperature advection and vertical entrainment/diffusion all contributed to the onset of the event, and that zonal advection played the dominant role during the decay of the event and the transition to La Niña. The net surface heat flux acts as a damping during the development stage, but plays a critical role in the decay of El Niño and the transition to the following La Niña.

The GODAS heat budget closure is generally poor for strong La Niñas. Despite the biases, the GODAS heat budget analysis tool is useful in monitoring and understanding the physical processes controlling the SST variability associated with ENSO. Therefore it has been implemented operationally at CPC in support of NOAA's operational ENSO forecasting.

Paper published

Huang, B., Y. Xue, D. Zhang, A.Kumar and M. J. McPhaden 2010: The NCEP GODAS ocean analysis of the tropical pacific mixed layer heat budget on seasonal to interannual time scales. *J. Climate*, Early Online Release (doi: 10.1175/2010JCLI3373.1).

Correspondence to: Yan Xue, Climate Prediction Center, NOAA/NWS/NCEP, Camp Springs, MD, 20746;
E-mail: yan.xue@noaa.gov

US National Oceanic and Atmospheric Administration
Climate Test Bed Joint Seminar Series
NCEP, Camp Springs, Maryland, 15 December 2009

Reconstruction of 20th Century North American Droughts Reveals a Key Role for Atlantic Basin Temperatures

Sumant Nigam
Department of Atmospheric & Oceanic Science and
Earth System Science Interdisciplinary Center (ESSIC)
University of Maryland, College Park, MD

ABSTRACT

The Great Plains of North America are susceptible to multi-year droughts, such as the 1930s 'Dust Bowl'. The droughts have been linked to SST variability in the Pacific and the Atlantic but the relative contribution of the basins in generation of prominent 20th century droughts (and wet episodes) is yet to be evaluated, in part, because the SST-forced dynamical models of the atmosphere – a common investigative tool – remain challenged in simulation of regional hydroclimate variability.

Here we adopt a statistical approach rooted in a new spatiotemporal analysis of 20th century SST variations and related drought links, which leads to remarkable reconstruction of the major dry and wet episodes over North America; attesting to the extent of the SST influence and facilitating evaluation of the basin contributions.

We find the Atlantic SSTs, tropical and extratropical, to be particularly influential; more than previously indicated, and often, more than the Pacific ones. Statistical drought reconstruction is provided a dynamical foundation from the extraction of SST-circulation links from a nearly century-long circulation record based, in part, on the recent upper-air meteorological analysis of the 1908-1948 period. The links show modulation of moisture transports to be important for drought generation, particularly in the fall. Rudimentary decadal projections based on phase-persistence of multidecadal SST variability suggest wetness over the central-northern Plains in spring-summer and drought conditions in fall.

Pacific and Atlantic SSTs evidently exert a profound influence on North American hydroclimate on decadal timescales, especially, in spring and fall; an influence not fully represented in present-day dynamical models of the atmosphere.

Paper published

Ruiz-Barradas, A. and S. Nigam, 2010: Great Plains precipitation and its SST links in 20th century climate simulations, and 21st and 22nd century climate projections. *J. Climate*, Early Online Release (doi: 10.1175/2010JCLI3173.1).

Correspondence to: Sumant Nigam, Department of Atmospheric & Oceanic Science and Earth System Science Interdisciplinary Center (ESSIC), University of Maryland, College Park, MD; E-mail: nigam@atmos.umd.edu

ANNEXES

Paper published

Murtugudde, R., 2009: Regional Earth System prediction: a decision-making tool for sustainability? *Current Opinion in Environmental Sustainability*. **1**, Elsevier, 37-45.

Huang, B., Y. Xue, D. Zhang, A.Kumar and M. J. McPhaden 2010: The NCEP GODAS Ocean Analysis of the Tropical Pacific Mixed Layer Heat Budget on Seasonal to Iinterannual Time Scales. *J. Climate*, Early Online Release.

Ruiz-Barradas, A. and S. Nigam, 2010: Great Plains Precipitation and its SST Links in 20th Century Climate Simulations, and 21st and 22nd Century Climate Projections. *J. Climate*, Early Online Release.

NOAA Climate Test Bed Joint Seminar Series
Extended Summaries Collection Volume

1. Assessment of Improvement in Climate Prediction with Outstanding R&D Needs (2009-2010)
   http://www.weather.gov/ost/climate/STIP/FY10CTBSeminars/CollectionVol_FY10CTBJS.pdf

2. Research to Operation and Operation to Research (2008-2009)
   http://www.weather.gov/ost/climate/STIP/FY09CTBSeminars/CollectionVol_FY09CTBJS.pdf

3. CFS as a Prediction System and Research Tool (2007-2008)
   http://www.weather.gov/ost/climate/STIP/CTB-COLA/ctb-cola_seminar_summaries.pdf